Metabolic reprogramming of cancer cells by JMJD6-mediated pre-mRNA splicing is associated with therapeutic response to splicing inhibitor

Carolyn Jablonowski[1#], Waise Quarni[1#], Shivendra Singh[1], Haiyan Tan[2], Dhanushka Hewa Bostanthirige[1], Hongjian Jin[3], Jie Fang[1], Ti-Cheng Chang[2], David Finkelstein[3], Ji-Hoon Cho[2], Dongli Hu[1], Vishwajeeth Pagala[2], Sadie Miki Sakurada[4], Shondra M. Pruett-Miller[4], Ruoning Wang[5], Andrew Murphy[1], Kevin Freeman[6], Junmin Peng[2,9], Andrew M Davidoff[1,7,8], Gang Wu[3], Jun Yang[1,7,8, 9]

[1]Department of Surgery, St Jude Children's Research Hospital, Memphis, TN38105, USA

[2]Center for Proteomics and Metabolomics, Department of Structural Biology, Department of Developmental Neurobiology, St Jude Children's Research Hospital, Memphis, TN38105, USA

[3]Center for Applied Bioinformatics, St Jude Children's Research Hospital, Memphis, TN38105, USA

[4]Department of Cell and Molecular Biology, St. Jude Children's Research Hospital, Memphis, TN 38105, USA.

[5]Center for Childhood Cancer and Blood Disease, Abigail Wexner Research Institute, Nationwide Children's Hospital, 700 Children's Drive, Columbus, OH 43205, USA.

[6]Genetics, Genomics & Informatics, The University of Tennessee Health Science Center (UTHSC), Memphis, TN 38103, USA.

[7]St Jude Graduate School of Biomedical Sciences, St Jude Children's Research Hospital, TN 38105

[8]Department of Pathology, College of Medicine, The University of Tennessee Health Science Center, 930 Madison Ave, Suite 500, Memphis, TN 38163

#equal contribution

[9]Correspondence: Jun.Yang2@stjude.org

The authors declare no potential conflicts of interest

Abstract

Dysregulated pre-mRNA splicing and metabolism are two hallmarks of MYC-driven cancers. Pharmacological inhibition of both processes has been extensively investigated as potential therapeutic avenues in preclinical and clinical studies. However, how pre-mRNA splicing and metabolism are orchestrated in response to oncogenic stress and therapies is poorly understood. Here, we demonstrate that Jumonji Domain Containing 6, Arginine Demethylase and Lysine Hydroxylase, JMJD6, acts as a hub connecting splicing and metabolism in MYC-driven neuroblastoma. JMJD6 cooperates with MYC in cellular transformation by physically interacting with RNA binding proteins involved in pre-mRNA splicing and protein homeostasis. Notably, JMJD6 controls the alternative splicing of two isoforms of glutaminase (GLS), namely kidney-type glutaminase (KGA) and glutaminase C (GAC), which are rate-limiting enzymes of glutaminolysis in the central carbon metabolism in neuroblastoma. Further, we show that JMJD6 is correlated with the anti-cancer activity of indisulam, a "molecular glue" that degrades splicing factor RBM39, which complexes with JMJD6. The indisulam-mediated cancer cell killing is at least partly dependent on the glutamine-related metabolic pathway mediated by JMJD6. Our findings reveal a cancer-promoting metabolic program is associated with alternative pre-mRNA splicing through JMJD6, providing a rationale to target JMJD6 as a therapeutic avenue for treating MYC-driven cancers.

67 **Introduction**

68 Metabolic reprogramming is a hallmark of cancer[1-3] which allows rapidly proliferating tumor cells to
69 acquire nutrients to meet their bioenergetic, biosynthetic, and redox demands[4]. One of the primary driving
70 forces in reprograming cancer cell metabolism is the deregulated MYC family proto-oncogenes (*C-MYC*,
71 *MYCN,* and *MYCL*)[5], which are known to encode master transcriptional factors that regulate metabolic
72 gene expression. MYC coordinates nutrient acquisition to produce ATP and key cellular building blocks
73 that increase cell mass and promote DNA replication and cell division[6]. The increase in total RNA and
74 protein synthesis by overactive MYC signaling leads to dysregulation of macromolecular processing
75 machineries including the spliceosome[7], and consequently pre-mRNA splicing[8-10], another hallmark of
76 MYC-driven cancers[7,9-12], for the purpose of cellular stress adaptation. *MYCN* amplification is one of the
77 most important biological features of high-risk neuroblastoma[13]. Transgenic mouse and zebrafish models
78 have demonstrated that MYCN is a neuroblastoma driver[14,15]. In tumors without *MYCN* amplification, *C-*
79 *MYC* is overexpressed, further indicating that neuroblastoma is a MYC-driven cancer. The metabolic
80 dependency of neuroblastoma has been widely studied by us and others[16-23]. A larger number of splicing
81 changes have also been noticed in high-stage neuroblastomas[24-26]. Splicing alterations lead to a
82 spliceosomal vulnerability that provides a new opportunity to develop transformative therapies by
83 disrupting aberrant pre-mRNA splicing[7,9-12]. We and others have shown that targeting the splicing factor
84 RBM39 by indisulam, a "molecular glue" that bridges RBM39 to E3 ubiquitin ligase DCAF15 for
85 proteasomal degradation, achieved significant anti-tumor activity in neuroblastoma models[27,28].
86 Disruption of spliceosome by Pladienolide B also resulted in significant anti-tumor effect in
87 neuroblastoma models[26] However, how the dysregulated pre-mRNA splicing machinery and metabolism
88 are orchestrated in MYC-driven neuroblastoma has not been well elucidated. Whether metabolism
89 modulates the anti-cancer effect of splicing inhibition remains to be answered.

90 Next-generation sequencing studies have revealed only a few recurrent somatic mutations in
91 neuroblastoma at the time of diagnosis[29,30]. However, copy number alterations of chromosomal segments
92 such as 17q gain, 1p36 or 11q23 loss frequently occur in high-risk neuroblastoma. While attempts to
93 understand the functions of individual genes in these chromosomal segments have been reported (i.e.,
94 BIRC5[31], PHB[32], PPM1D[33], TRIM37[34] in 17q; ARID1A[35], CAMTA1[36], CASZ1[37], CHD5[38-40], KIF1Bβ[41-
95 43], miR-34a[44], RUNX3[45] in 1p36), the biological consequences of these genetic events in MYC-driven
96 tumors still remain largely unknown. Gain of 17q is the most frequent genetic event in high-risk
97 neuroblastoma and is associated with *MYCN* amplification[46]. In addition, in the transgenic *MYCN* mouse
98 model of neuroblastoma, the chromosomal locus syntenic to human 17q is partially amplified[47], indicating
99 that chromosome 17q is needed for MYC-mediated tumorigenesis.

100 JMJD6 is a JmjC domain–containing nuclear protein with iron- and 2-oxoglutarate–dependent
101 dioxygenase activity[48], whose coding gene is located on chromosome 17q25. While the histone arginine
102 demethylase activity of JMJD6 that catalyzes demethylation of H4R3me1/me2 is controversial[49], JMJD6
103 is a lysyl-5-hydroxylase that catalyzes 5-hydroxylation on specific lysine residues of target proteins[50].
104 JMJD6 has pleiotropic functions in normal physiology and in cancer[51-54]. We previously found that
105 JMJD6 is essential for the survival of neuroblastoma cells (including *MYCN*-amplified and *C-MYC*–
106 overexpressed cells)[55], which was further validated by an independent study[56], indicating that
107 neuroblastoma has JMJD6 dependency. However, the exact mechanism of JMJD6 in MYC-driven cancers
108 remains elusive. One study has shown that JMJD6 and BRD4 co-bind at antipause enhancers, regulating
109 promoter-proximal pause release of a large subset of transcription units[57]. By harnessing a similar
110 mechanism, JMJD6 promotes cell survival of glioblastoma *in vivo*[58]. These findings are particularly
111 interesting because BRD4 occupies exceptionally large super-enhancers associated with genes, including
112 *C-MYC* and *MYCN*[59-61], and the expression of those enhancers can be disrupted by BRD4 inhibitors, which
113 have a potent antitumor effect[59-62]. Here we show a new mechanism by which JMJD6 promotes
114 tumorigenesis mediated by the MYC oncogene in that JMJD6 interacts with a subset of RNA binding
115 proteins including RBM39 in neuroblastoma cells and regulates the alternative splicing of metabolic genes
116 that are involved in mitochondrial metabolism. "Glutamine addiction" is one key feature of MYC-driven
117 tumors. Glutaminase (GLS) is the enzyme responsible for conversion of glutamine to glutamate in the
118 process of glutaminolysis to feed the tricarboxylic acid (TCA) cycle and has two splice isoforms, GAC
119 (glutaminase C) and KGA (kidney-type glutaminase). We show that JMJD6 controls the alternative
120 splicing of KGA and GAC, and, consequently, impacts the central carbon metabolism in neuroblastoma.
121 Further we show that JMJD6 is correlated with the anti-cancer activity of indisulam, a "molecular glue"
122 that degrades the splicing factor RBM39. The indisulam-mediated cancer cell killing is at least partly
123 dependent on the glutamine-related metabolic pathway mediated by JMJD6. Our findings demonstrate a
124 new mechanism by which JMJD6 coordinates metabolic programs and alternative pre-mRNA splicing,
125 providing a rationale to target JMJD6 as a therapeutic target for MYC-driven cancers.
126

127 **Results**

128 **The essential genes for neuroblastoma cell survival on chromosome 17q target pre-mRNA splicing**
129 **and metabolism**

130 An incomplete understanding of the biological consequences of chromosome 17q gain remains a barrier
131 to the understanding of high-risk neuroblastoma. 1132 genes are located on 17q (**Supplementary table**
132 **1**). We surmised that some of the 17q genes are particularly important for neuroblastoma cell survival.

133 Analysis of the cancer dependency genes in neuroblastoma cell lines screened with the Avana sgRNA
134 library[63] revealed that 114 were essential to neuroblastoma (mean score <-0.4) (**Figure 1a**,
135 **Supplementary table 2**). Protein interaction network analysis followed by functional annotation revealed
136 that proteins encoded by these 114 essential genes formed distinct but interconnected modules including
137 RNA splicing (i.e., SRSF2, DDX5, DDX42, DHX8), mitochondrial metabolism (i.e., NDUFA8, COX11,
138 SLC25A10, SLC35B1), protein homeostasis (i.e., UBE2O, PSMB3, PSMC5), DNA repair (i.e., BRIP1,
139 BRCA1, RAD51C, RAD51D) and transcriptional regulation (i.e., PHF12, CBX1, SMARCE1, MED1),
140 as well as endocytosis (i.e., CHMP6, CTLC, EPN3, HGS, SNF8, VPS25) (**Figure 1b**). Children aged ≥18
141 months with metastatic disease and patients with MYCN amplification tumors are classified as high-risk,
142 which requires a multimodal therapy including induction chemotherapy, surgical resection of primary
143 disease, consolidation with high-dose chemotherapy and stem cell rescue, radiotherapy, and post-
144 consolidation treatment with cis-retinoic acid and immunotherapy[64]. Using these 114 genes as a signature,
145 we found that 81 of them were highly expressed in high-risk neuroblastomas, which were enriched with
146 MYCN amplification (**Figure 1c**). Correspondingly, neuroblastomas with high expression levels of this
147 gene signature were associated with a poorer event-free (time from treatment until the cancer progresses)
148 and overall survival (time from treatment to death) of patients in two large clinic cohorts (**Figure 1d, e,**
149 **Supplemental Figure 1**). Interestingly, in low-risk neuroblastoma patients, high expression of the 114
150 essential genes was associated with poor event-free and overall survival, while no difference was observed
151 in high-risk patients (**Supplemental Figure 2**). These data demonstrate that 17q genes are involved in
152 essential biological processes and highly expressed in high-risk neuroblastomas. Nevertheless, the 114
153 essential genes cannot further stratify the high-risk patients.
154
155 **JMJD6 is required for neuroblastoma growth**
156 *JMJD6* was among these 114 essential genes. To understand the role of JMJD6, we examined the genetic
157 features of *JMJD6* in neuroblastoma and other types of cancers. Among the genes encoding JmjC-domain
158 containing proteins, *JMJD6* was the only one that was frequently amplified in neuroblastoma (**Figure 2a**).
159 High *JMJD6* expression was associated with poor event-free outcome, as shown by Kaplan-Meier analysis
160 (**Figure 2b**). Further analysis of JMJD6 expression in low-risk and high-risk patients showed that high
161 levels of JMJD6 expression was associated with poor event-free and overall survival in both low-risk and
162 high-risk patients (**Supplementary Figure 3a-d**), indicating that JMJD6 is high-risk factor regardless of
163 disease status. To examine whether *JMJD6* amplification is limited to specific tumor types, we explored
164 genomic data from different cancers using the cBioportal program[65]. *JMJD6* was amplified across
165 multiple types of adult cancers such as breast and liver cancer (**Supplementary Figure 4a**), and correlated

166 with worse relapse-free survival (**Supplementary Figure 4b**). We further compared the RNA-seq
167 expression of *JMJD6* in 2337 samples across over 20 pediatric cancer subtypes and found that *JMJD6*
168 showed the highest expression levels in neuroblastoma (**Supplementary Figure 4c**), suggesting that
169 JMJD6 might be particularly important in neuroblastoma. We validated this hypothesis using shRNA
170 knockdown of JMJD6 in *MYCN* amplified cells (BE2C, SIMA, KELLY, IMR32) and non-*MYCN*
171 amplified cells (SK-N-AS and CHLA20). The results showed that loss of JMJD6 greatly reduced the
172 colony numbers in all tested cell lines (**Figure 2c, and Materials and Methods**), demonstrating that
173 JMJD6 is essential to neuroblastoma cells regardless of *MYCN* amplification. Neuroblastic tumors
174 comprise a histologic spectrum that ranges from less-differentiated neuroblastoma to well-differentiated
175 ganglioneuroma. The extent of differentiation in the tumor cells is correlated with prognostic
176 significance[66]. We noticed that the loss of JMJD6 led to neurite outgrowth (**Supplementary Figure 4d**),
177 a unique structure of neuroblastoma cells differentiating *in vitro*. This morphologic change suggests that
178 JMJD6 is required to regulate cellular differentiation. Lastly, we validated that JMJD6 is essential to
179 neuroblastoma growth in *MYCN* amplified (BE2C) and C-MYC overexpressed (SK-N-AS) xenograft
180 models (**Figure 2d, e**). Taken together, these data demonstrate that loss of JMJD6 function impedes
181 neuroblastoma cell survival and tumor growth.
182
183 **JMJD6 promotes MYC-mediated cellular transformation**
184 Next, we investigated whether gain of function of JMJD6 could facilitate MYC-mediated oncogenic
185 transformation. To test this, we used a NIH3T3 transformation assay that provides a straightforward
186 method to assess the transforming potential of an oncogene, which may lead to morphological
187 transformation and loss of contact inhibition, a typical feature of cellular transformation. Like the GFP
188 control (**Supplementary Figure 5a**), we found that NIH3T3 cells with overexpressed JMJD6 stopped
189 proliferation after being confluent (**Supplementary Figure 5b**), indicating JMJD6 alone is unable to
190 transform NIH3T3 cells. However, overexpression of MYCN induced foci formation with enhanced cell
191 death (**Supplementary Figure 5c**). Importantly, NIH3T3 cells with overexpressed MYCN and JMJD6
192 lost contact inhibition, accompanied with morphological change, and formed larger foci (**Supplementary**
193 **Figure 5d**), indicating that JMJD6 enhances MYCN activity to transform NIH3T3 cells. Interestingly,
194 MYCN alone also reprogramed metabolism of NIH3T3 cells as shown by the color change of the media,
195 which was largely rescued by co-expression of JMJD6 (**Supplementary Figure 5e**), suggesting that cells
196 with enhanced lactate production by MYCN were directed to oxidative phosphorylation by JMJD6. It is
197 believed that the cell of origin of neuroblastoma is the progeny of neural crest cells[67,68]. We therefore
198 tested the role of JMJD6 in MYC-mediated transformation using JoMa1[69], a cell line derived from murine

199 neural crest, by transducing GFP, JMJD6, MYCN and JMJD6/MYCN (**Figure 2f**). While JMJD6 showed
200 no difference from GFP control in regulating cell proliferation, MYCN slightly enhanced cell proliferation
201 (**Figure 2g**). However, the combination of JMJD6 and MYCN remarkably increased cell proliferation,
202 mirrored by the colony formation assay which showed JMJD6/MYCN induced rapid growth of colonies
203 with distinct transformation morphology (**Figure 2g, h**). Implantation of each group into immune-
204 deficient mice led to tumor development of MYCN and JMJD6/MYCN groups (**Figure 2i**). However,
205 JMJD6/MYCN group tumors appeared to grow faster than the MYCN alone tumors. Taken together, these
206 data indicate that JMJD6 enhances the MYC-mediated transformation, demonstrating the oncogenic role
207 of JMJD6.
208
209 **JMJD6 regulates pathways engaged in pre-mRNA splicing and mitochondrial biogenesis in**
210 **neuroblastoma**
211 We surmised that loss of function of genes in the same functional module/pathway may induce similar
212 effects across different cell lineages, which in turn corroborates the hypothesis that JMJD6 is a player in
213 that signaling pathway. To test this hypothesis, we analyzed the dependency correlation of *JMJD6*
214 knockout and other genes (defined as co-dependency genes if they are positively correlated), by using the
215 DepMap data (https://depmap.org) that includes genome-wide knockout in 1027 cell lines of more than
216 20 cancer types (**Supplementary Table 3**), followed by pathway enrichment. The data showed that
217 JMJD6 co-dependency genes were significantly and positively correlated with spliceosome/mRNA
218 splicing (i.e., RBM39, SF3B1), ubiquitin-mediated proteolysis and endocytosis and a number of 17q25
219 genes, (**Figure 3a, c**), which mirrored the pathway network of 17q essential genes in neuroblastoma
220 (**Figure 1b**). JMJD6 knockout was negatively correlated with the knockout of genes housed at
221 chromosome 1p, which is frequently deleted in high-risk neuroblastoma, and oxidative phosphorylation
222 as well as protein translation (**Figure 3b, d**).
223
224 BRD4 is known to regulate MYC expression[61,70]. Previous studies have shown that JMJD6 and BRD4
225 interact to regulate gene transcription[56,58,71], suggesting that JMJD6 might directly modulate MYC
226 expression. To assess this possibility, we knocked down *JMJD6* in neuroblastoma cell lines BE2(C) and
227 SK-N-AS, which express *MYCN* and *C-MYC*, respectively, for RNA-seq analysis. The sequencing data
228 were analyzed for differential gene expression (**Supplementary Table 4**). Interestingly, loss of JMJD6
229 showed minimal impact on expression of *MYCN* in BE2C cells or *C-MYC* in SK-N-AS cells
230 (**Supplementary Figure 6a**), and western blot analysis did not show alteration of MYCN expression
231 although C-MYC protein was slightly downregulated by loss of JMJD6 (**Supplementary Figure 6b**).

232 However, BRD4 inhibitors drastically inhibited both MYCN and C-MYC expression in neuroblastoma
233 cells[59-61], suggesting that JMJD6 inhibition has a distinct effect from the BRD4 inhibition. Gene set
234 enrichment analysis for pathway engagement for the genes commonly downregulated or upregulated in
235 both cell lines revealed that loss of JMJD6 most significantly repressed the expression of genes involved
236 in pre-mRNA splicing, histones, and cell cycle G1/S checkpoint (**Figure 3e**), and enhanced the pathways
237 involved in mitochondrial functions and heat shock response (**Figure 3e**). Interestingly, the genes
238 transcribed from the mitochondrial genome were elevated in both cell lines (**Supplementary Figure 6c**),
239 suggesting that JMJD6 directly or indirectly regulates the transcription of mitochondrial genome. These
240 data are consistent with the co-dependency pathways of JMJD6 (**Figure 3a-d**). Depletion of JMJD6 in
241 both cell lines led to the downregulation of MYC signaling pathways (**Supplementary Figure 7a**),
242 although ranked behind the pathways of splicing and metabolism, suggesting that the MYC pathways are
243 not primarily regulated by JMJD6. These data indicate that JMJD6 does not regulate the gene expression
244 of the MYC family of transcription factors but might indirectly regulate the MYC pathway. Nevertheless,
245 loss of JMJD6 induced an induction of gene signatures related to axon, neuron projection, and Schwann
246 cell differentiation (**Supplementary Figure 7b**), which is consistent with the induction of neurite
247 outgrowth observed in BE2C cells after JMJD6 knockdown (**Supplementary Figure 4d**), indicative of
248 neuroblastoma cell differentiation.
249
250 To verify if JMJD6 regulates pre-mRNA splicing, we analyzed the RNA-seq using two algorithms[72]. The
251 first one is event-based analysis to identify the altered exon splicing (**Figure 3f**). We found that
252 knockdown of JMJD6 dominantly affects the exon skipping (SE) although other splicing events were also
253 altered, albeit with a much smaller number (**Figure 3f**). Pathway analysis of common events in both BE2C
254 and SK-N-AS cells demonstrated that genes involved in metabolism and splicing are the most significantly
255 affected by loss of function of JMJD6 (**Figure 3g**). Using the second algorithm of RNA splicing analysis
256 previously developed (**Figure 3h**) that allows discovery of new isoforms of genes generated through
257 alternative splicing[72], we identified 580 genes in BE2C cells and 1018 genes in SK-N-AS cells undergoing
258 alternative splicing after JMJD6 knockdown, 133 of which were shared by both (**Figure 3h,**
259 **Supplementary Fig. 8, Supplementary Table 5**). The alternatively spliced genes were involved in a
260 variety of pathways (**Supplementary Table 6**). Among the 133 commonly alternatively spliced genes,
261 KEGG pathway enrichment analysis showed that metabolic pathway genes were the only ones
262 significantly enriched (**Figure 3f**), most of which are involved in mitochondrial bioenergetics and folate
263 metabolism (**Figure 3h**). Collectively, these data demonstrate that JMJD6 regulates RNA splicing of

264 genes engaged in mitochondrial metabolism, being one of the key mediators of the 17q locus activity in
265 neuroblastoma.
266
267 **JMJD6 regulates alternative splicing of glutaminolysis gene GLS**
268 Overactive MYC signaling leads to altered macromolecular processing machineries in response to an
269 increase in total RNA and protein synthesis[7]. MYC is also a master regulator of cancer metabolism
270 involved in ribosomal and mitochondrial biogenesis, glucose and glutamine metabolism and lipid
271 synthesis, leading to the acquisition of bioenergetic substrates enabling the cancer cell to grow and
272 proliferate[73-75]. "Glutamine addiction" is one feature of MYC-driven cancer[76]. The pre-mRNA splicing
273 altered by JMJD6 knockdown included *GLS*, the key enzyme of glutaminolysis, prompting us to
274 investigate the *GLS* splicing mediated by JMJD6 knockdown. GLS is known to catalyze the conversion
275 of glutamine to glutamate, and is alternatively spliced to form two isoforms, GAC and KGA[77], with
276 different cellular localization and catalytic capacities[78]. The GAC isoform is more frequently upregulated
277 in cancer cells than KGA[79], and has been shown to be regulated by MYC[80-82], leading to a "glutamine
278 addiction" phenotype in MYC-driven tumors[76]. We found that loss of JMJD6 led to a splicing switch from
279 the GAC isoform (with exons 1-15) to the KGA isoform (with exons 1-14 and 16-19) (**Figure 4a,**
280 **Supplementary Fig. 9**), which was further confirmed by isoform-specific RT PCR (**Figure 4b**). We then
281 investigated the expression of GAC/KGA at the protein levels after JMJD6 knockdown. Western blot
282 showed that the KGA isoform was increased after JMJD6 knockdown in all three tested cell lines, C-MYC
283 overexpressed SK-N-AS, BE2C and SIMA with MYCN amplification (**Figure 4c**). Then we further
284 validated the JMJD6 effect on GLS isoform expression by using a luciferase reporter that indicates the
285 isoforms of GAC and KGA. Indeed, JMJD6 knockdown significantly increased the expression of the KGA
286 reporter (**Figure 4d**). RNA-immunoprecipitation showed that JMJD6 bound to *GLS* RNA (**Figure 4e**),
287 suggesting that JMJD6 may directly regulate the splicing of *GLS*. We reasoned that if the regulation of
288 *GLS* splicing by JMJD6 was a bone fide mechanism, the expression levels of *JMJD6* would correlate with
289 the levels of *GAC/KGA* in tumors. Indeed, *JMJD6* was positively correlated with *GAC* and negatively
290 correlated with *KGA* in two independent neuroblastoma cohorts (**Figure 4f**), supporting the hypothesis
291 that JMJD6 is required to maintain the high ratio of *GAC*/*KGA* in cancer cells by controlling their
292 alternative splicing. Clinical relevance of *GAC* and *KGA* in neuroblastoma was evidenced by the findings
293 that high *GAC* was associated with a worse event-free survival and high *KGA* was associated with a better
294 event-free survival (**Figure 4g, h**), suggesting that the *GAC*/*KGA* ratio may play a role in cancer
295 progression.
296

297 **GAC and KGA are both important for cell survival**

298 To understand if GAC and KGA play distinct roles in neuroblastoma cells, we transduced GAC or KGA
299 into BE2C and SKNAS cells. However, introduction of either GAC or KGA in BE2C cells or SKNAS
300 cells promoted colony formation (**Figure 5a-d**), indicating that enhanced glutaminolysis by either GAC
301 or KGA overexpression is pro-proliferative. Interestingly, RNA-seq analysis revealed that GAC and KGA
302 share common targets but also have distinct targets in both BE2C and SKNAS cells (**Supplemental**
303 **Figure 10a, b**). KEGG pathway analysis of the commonly upregulated genes by GAC and KGA showed
304 that both GAC and KGA promoted the PI3K-AKT and MAPK pathways in both cell lines (**Figure 5e, f**).
305 However, for the genes commonly downregulated by GAC and KGA, KEGG pathway showed that
306 calcium signaling was significantly downregulated in BE2C cells while steroid biosynthesis was
307 significantly downregulated in SKNAS cells (**Figure 5e, f**). Then we examined that GAC- and KGA-
308 specific effects in both cell lines. In BE2C cells, GAC expression promoted Hedgehog, Hippo and Notch
309 signaling pathways (**Supplemental Figure 10c**), while KGA expression promoted mitophagy signaling
310 pathway (**Supplemental Figure 10d**). In SKNAS cells, GAC expression promoted PI3K-AKT and Hippo
311 pathways (**Supplemental Figure 10e**) and KGA expression promoted TNF signaling pathway
312 (**Supplemental Figure 10f**). Thus, while GAC and KGA catalyzes the same chemical reaction by
313 converting glutamine to glutamate, they also induce non-redundant cellular responses in neuroblastoma
314 cells, suggesting that both isoforms might be important for neuroblastoma cells. Indeed, knockdown of
315 both isoforms (GLS) showed a greater cancer cell killing phenotype than that of GAC or KGA alone did
316 (**Figure 5g-i**).
317

318 **JMJD6 forms an interaction network with proteins involved in splicing and protein synthesis**

319 To understand the mechanism of JMJD6 in regulating splicing in neuroblastoma, we performed an
320 unbiased identification of JMJD6 interacting partners by introducing a flag-tagged JMJD6 into SK-N-AS
321 and BE2C cells, followed by immunoprecipitation to pull down the JMJD6 associated complex and
322 protein identification with mass spectrometry (**Figure 6a, Supplementary Table 7**). We found that
323 JMJD6 mainly interacted with two classes of proteins which are involved in RNA splicing and protein
324 synthesis in both cell lines, respectively (**Figure 6a, Supplementary Figure 11**). We then validated the
325 interactions of JMJD6 with splicing factors using immunoprecipitation and western blot, and
326 demonstrated JMJD6 formed a complex with these RNA binding proteins, including RBM39 (**Figure 6b**),
327 a therapeutic target of high-risk neuroblastoma[27]. Since JMJD6 also interacted with several molecules
328 involved in protein translation, we investigated if JMJD6 also regulates protein synthesis by using an
329 approach, Click-IT AHA to label the newly synthesized proteins, followed by western blot assessment

330 (**Figure 6c**). Interestingly, overexpression of JMJD6 greatly reduced total protein synthesis (**Figure 6c**),
331 suggesting that JMJD6 may antagonize protein production.
332
333 Then we determined if the splicing factors interacting with JMJD6 also regulate GLS isoform expression.
334 Among the splicing factors with which JMJD6 interacted, CPSF6 has been previously shown to regulate
335 the alternative splicing of *GLS*[83]. We validated the function of CPSF6 in neuroblastoma cells and found
336 that, indeed, loss of CPSF6 led to a dramatic switch from GAC to KGA in BE2C and SK-N-AS cells
337 (**Figure 6d, 6e**). Previous studies showed that JMJD6 and U2AF2 (U2AF65) interact to regulate
338 splicing[50,84]. We also found that knockdown of U2AF2 resulted in a similar phenotype to JMJD6
339 knockdown in that the expression of KGA isoform was greatly increased in both cell lines (**Figure 6d,**
340 **6e**). These data collectively support the functions of JMJD6 in regulating the splicing of metabolic genes
341 and protein homeostasis in MYC-driven neuroblastoma.
342
343 **JMJD6 regulates production of TCA intermediates and nucleoside triphosphate**
344 To further dissect the biological consequences of loss of function of JMJD6, we created stable JMJD6
345 knockout clones (**Supplementary Figure 12**) and defined the metabolite spectrum affected by loss of
346 function by using liquid chromatography with tandem mass spectrometry (LC-MS/MS). JMJD6 knockout
347 greatly reduced the production of tricarboxylic acid cycle (TCA) intermediates (i.e., oxoglutarate,
348 fumarate) and nucleoside triphosphate (ATP, CTP, GTP) (**Figure 7a**), indicating that JMJD6 is a key
349 bioenergetics regulator in cancer cells. Pathway analysis revealed that the reduced metabolites were
350 involved in the Warburg effect, TCA, pentose phosphate pathway, and mitochondrial electron transport
351 chain (**Figure 7b**), all of which are critical for providing cancer cell bioenergetics for proliferation and
352 survival. Oxoglutarate (α-ketoglutarate) and fumarate are downstream products of glutaminolysis (**Figure**
353 **7c**). We reasoned that cellular metabolites such as glutamate and oxoglutarate may predict the cytotoxic
354 effect of loss-of-function of JMJD6. If cells have higher levels of glutamate and oxoglutarate, they might
355 be less dependent on JMJD6 due to their higher capacity of buffering against reduced glutaminolysis. To
356 test this hypothesis, we used DepMap data that included 225 metabolites in 928 cancer cell lines from
357 over 20 lineages[85], and analyzed the correlation of each metabolite with *JMJD6* gene dependency. The
358 data showed that cells with high levels of AMP, glutamate, alanine, 2-hydroxyglutarate and 2-oxoglutarate
359 were more resistant to JMJD6 knockout, while cells with high levels of lactose and sucrose were more
360 sensitive to JMJD6 knockout (**Figure 7d, Supplementary Table 8**). High levels of AMP activate AMP
361 kinase (AMPK), consequently leading to enhanced fatty acid oxidation to stimulate ATP production while
362 alanine can be converted to pyruvate to provide acetyl-CoA to fuel the TCA cycle (**Figure 7c**). Therefore,

363 high levels of AMP and alanine may provide cells alternative bioenergetics sources for survival. These
364 data further indicate that JMDJ6 function is wired into the regulation of mitochondrial metabolism.
365
366 **JMJD6 determines the efficacy of indisulam, a molecular glue degrading splicing factor RBM39**
367 Dysregulated splicing as a vulnerability of MYC-driven cancers provides a rationale to target
368 neuroblastoma by using splicing inhibitors as a therapeutic approach. We and others have recently
369 reported that indisulam, a "molecular glue" that selectively degrades the splicing factor RBM39, is
370 exceptionally effective at causing tumor regression in multiple high-risk neuroblastoma models without
371 overt toxicity[27,28], suggesting indisulam has translational potential. Understanding the factors determining
372 the efficacy of indisulam or any other drug is critical for developing precision therapy, combination
373 therapy or preventing therapy resistance. In addition to complexing together (**Figure 6a, b**), JMJD6 and
374 RBM39 exhibit significant correlation of co-dependency in cancer cells, namely, cancer cells have similar
375 dependency on JMJD6 and RBM39 for survival (**Supplementary Table 3, Figure 8a**). These data
376 indicate that JMJD6 may play a role in modulating the effect of indisulam. To test this hypothesis, we
377 performed GSEA to identify the differential pathways between indisulam-sensitive and indisulam-less
378 sensitive neuroblastoma cells. It turned out that histone lysine demethylase (HDM) genes, including
379 JMJD6, are present in the most significantly enriched gene signature in indisulam-sensitive cells (**Figure**
380 **8b, c, d**). Indeed, knockout of JMJD6 led to partial but significant resistance to indisulam treatment of
381 SK-N-AS cells (**Figure 8e-g**) and BE2C cells (**Figure 8h-j**), supporting that cells with high JMJD6
382 expression are more dependent on RBM39. Since we found that JMJD6 plays a key role in modulating
383 glutaminolysis, we tested if expression of GAC or KGA could affect the activity of indisulam.
384 Interestingly, overexpression of either GAC and KGA renders BE2C and SK-N-AS cells more resistant
385 to indisulam treatment (**Figure 8k-n**), suggesting that enhanced glutaminolysis may confer therapeutic
386 resistance to spliceosome inhibition.
387
388 **Discussion**
389 MYC is an oncogenic driver of many types of cancer and plays a pivotal role in regulating glycolysis,
390 glutaminolysis, nucleotide and lipid synthesis, and ribosome and mitochondrial biogenesis[6]. Recent
391 studies have revealed that there is also an interplay between MYC and pre-mRNA splicing machinery[7-
392 10,86-89]. Pre-mRNA splicing is an essential biological process catalyzed by the spliceosome to produce
393 mature mRNAs[90,91]. Over 90% of multiexon genes in the human genome undergo alternative splicing[92,93],
394 which significantly expands the diversity of the proteome and consequently impacts various biological
395 functions[94,95]. In this study, we found that the chromosome 17q locus, which is frequently gained in MYC-

396 driven cancers, houses numerous genes essential to cancer cell survival that are implicated in pre-mRNA
397 splicing, ribosome and mitochondrial biogenesis and other biological functions. Particularly, JMJD6,
398 which is located on 17q25 and is amplified in a number of cancer types, physically interacts with a subset
399 of splicing factors such as RBM39 and regulates the alternative splicing of metabolic genes. Depletion of
400 JMJD6 inhibits cancer cell proliferation and impedes tumor growth while overexpression of JMJD6
401 promotes MYC-mediated tumorigenesis, suggesting that JMJD6 and potentially other 17q genes have
402 oncogenic functions in cellular transformation. Previous studies suggest that JMJD6 and BRD4 interact
403 to regulate gene transcription[56,71]. However, our unbiased identification of the JMJD6 interactome only
404 identified a subset of proteins involved in mRNA splicing and protein translation in neuroblastoma cells,
405 suggesting that JMD6 may predominantly regulate protein homeostasis to facilitate MYC-mediated
406 transformation. Nevertheless, we cannot exclude the possibility that our immunoprecipitation conditions
407 were too stringent, leading to dissociation of proteins that loosely or dynamically bind to JMJD6.
408
409 MYC-induced metabolic reprogramming triggers cellular dependency on exogenous glutamine as a source
410 of carbon for mitochondrial membrane potential maintenance and macromolecular synthesis[2], leading to
411 "glutamine addiction"[2]. Glutaminolysis is a process by which GLS and GLS2 convert glutamine to
412 glutamate, which is, in turn, converted by glutamate dehydrogenase or transaminase to 2-oxoglutarate that
413 is further catabolized in the TCA cycle. Additionally, glutamate is a substrate for production of
414 glutathione, an important antioxidant. We previously showed that neuroblastoma relies on MYCN-
415 induced glutaminolysis for survival[20]. In this study, our RNA-seq barely detected the expression of *GLS2*
416 in the neuroblastoma cell models we used, indicating that GLS is the major enzyme that catalyzes
417 glutamine in these model systems. *GLS* has two isoforms, *GAC* and *KGA*, resulting from alternative
418 splicing. KGA is mainly localized in the cytoplasm while GAC is localized in mitochondria and has a
419 higher basal activity[78]. *GAC* mRNA levels strongly correlate with the conversion of glutamine to
420 glutamate, as a proxy for GAC activity[96]. The positive correlation of *JMJD6* and *GAC* suggests that the
421 JMJD6-high tumors have enhanced glutaminolysis activity. CSPF6 and the noncoding RNA *CCAT2* have
422 been reported to regulate the splicing of GLS isoforms[83,97]. Interestingly, we found that depletion of
423 JMJD6 leads to a *GLS* isoform switch from *GAC* to *KGA*, indicating that JMJD6 is involved in alternative
424 splicing of *GLS*. We further found that JMJD6 physically interacts with CPSF6 in a splicing network and
425 validated that loss of CPSF6 results in remarkable induction of the KGA isoform. We further validated
426 that other splicing factors such as U2AF2 also interact with JMJD6 to regulate the GLS isoform switch.
427 These data indicate that cancer cells can adjust metabolism through alternative splicing to produce
428 enzymes with distinct subcellular localization and activity that promote cellular transformation or

429 progression of an oncogenic phenotype. The cooperation of JMJD6 and MYC in cellular transformation
430 further supports the hypothesis that JMJD6 is needed for metabolic reprogramming triggered by MYC.
431 However, overexpression of either GAC or KGA promotes cell proliferation, suggesting that the switching
432 of KGA/GAC is a cellular fitness mechanism in response to interruption of the spliceosome by adjusting
433 the metabolic rate. Within the tumor microenvironment (i.e., replete and deplete oxygen and nutrient
434 supply) GLS activity is possibly finely tuned through splicing mechanism for adaption.
435
436 Additionally, we found that JMJD6 physically interacts with a subset of ribosomal proteins that are
437 responsible for protein translation. Interestingly, overexpression of JMJD6 reduces global protein
438 synthesis. A recent study showed that MYC overactivation leads to proteotoxic stress in cells by enhancing
439 global protein synthesis, consequently causing cell death[98]. The increased global protein synthesis by
440 MYC needs to be buffered through loss of DDX3X, a regulator of ribosome biogenesis and global protein
441 synthesis, for lymphomagenesis[98]. Our findings suggest that, besides the functions in regulating alternative
442 splicing for metabolism, JMJD6 is involved in MYC-mediated cell transformation by buffering unwanted
443 proteotoxic stress due to high rate of protein synthesis induced by MYC (**Figure 9**).
444
445 Neuroblastoma is responsible for as much as 15% of childhood cancer mortality[99]. With current intensive
446 multimodal therapies, 5-year survival rates for high-risk patients remain less than 50%[100-103]. In addition,
447 survivors of high-risk disease have a significant risk of developing long-term side effects including
448 subsequent malignant neoplasms due to cytotoxic chemotherapy and radiotherapy[104,105]. Unfortunately,
449 developing effective precision therapies against high-risk neuroblastoma has been challenging due to the
450 lack of targetable recurrent mutations in neuroblastoma[29,30,106]. Our previous study showed that indisulam,
451 the splicing inhibitor that targets RBM39, a JMJD6-interacting partner, induced a durable complete
452 response in multiple high-risk neuroblastoma models, supporting its potential use in future clinical trials.
453 Our current study showed that JMJD6 expression is positively correlated with the effect of indisulam, and
454 knockout of JMJD6 confers resistance to indisulam treatment. In line with the biological functions of
455 JMDJ6 in regulating GLS isoform expression and mitochondrial metabolism, overexpression of GAC or
456 KGA also caused resistance to indisulam treatment. These data indicate that JMJD6 could serve as a
457 biomarker that predicts response to indisulam or other splicing inhibitors.
458
459 **Limitation of the study**
460 Our study focused on the understanding of JMJD6 function in neuroblastoma cell lines. In the future, we
461 will consolidate our study by expanding our models to patient-derived xenografts, organoids, and

462 neuroblastoma genetic models, in comparison with non-cancerous cells. Although we have identified a
463 conserved interactome of JMJD6 in neuroblastoma cells, it remains to be determined whether it is
464 neuroblastoma-specific and essential to MYC-driven cancers. The genome-wide RNA binding by JMJD6
465 in cancer cells and normal cells coupled with isotope labeling to dissect the metabolic effect of JMJD6
466 will enhance our understanding of the biological functions of JMJD6, awaiting future studies. Inability to
467 target the enhanced pre-mRNA splicing of metabolic genes in MYC-driven cancer cells by pharmacologic
468 inhibition of JMJD6 is another limitation, due to lack of selective and potent JMJD6 inhibitors.
469
470 **Materials and Methods**
471
472 **Cell lines.** KELLY (ECACC, 92110411), SIMA (DSMZ, ACC164), BE2C (ATCC, CRL2268), IMR32
473 (ATCC, CCL127), SK-N-AS (ATCC, CRL2137), CHLA20 (COG) were cultured in 1X RPMI1640
474 (Corning, 15-040-CV) supplemented with 10% Fetal Bovine Serum (Sigma-Aldrich, F2442), 1% L-
475 Glutamine (Corning, A2916801). NIH3T3 (ATCC, CRL1658) and 293T (ATCC, CRL3216) cells were
476 cultured in 1X DMEM supplemented with 10% Fetal Bovine Serum (Sigma-Aldrich, F2442), 1% L-
477 Glutamine (Corning, A2916801). All cells were maintained at 37 °C in an atmosphere of 5% CO_2. JoMa1
478 cells were kindly provided by Dr. Schulte (Department of Pediatric Oncology and Hematology, University
479 Children's Hospital Essen, Essen, Germany) were cultured in NCC Medium: DMEM (4.5 mg/ml Glucose,
480 L-Glutamine, Pyruvate): Ham's F12 (1:1) was supplemented with: 1% N2-Supplement (Invitrogen, no.
481 17502-048), 2% B27-Supplement (Invitrogen, no. 17504-044), 10ng/ml EGF (Invitrogen), 1ng/ml FGF
482 (Invitrogen), 100U/ml Penicillin–Streptomycin (Invitrogen) and 10% Chick-Embryo-Extract (Gemini
483 Bio-Products, CA). Neural crest culture medium was supplemented with 200 nM 4-OH-tamoxifen (Sigma
484 no. H7904) in routine culture to ensure nuclear localization of c-MycERT and JoMa1 cell proliferation.
485 JoMa1 cells were grown on cell culture flask/dish coated with fibronectin, NCC-medium supplemented
486 with 200nm 4-OHT was changed daily. Cells were passaged after 3–4 days in culture when 70%
487 confluence was reached (4 X 10^6 cells/10 cm dish).
488 All human-derived cell lines were validated by short tandem repeat (STR) profiling using PowerPlex®
489 16 HS System (Promega) once a month. Additionally, a polymerase chain reaction (PCR)-based method
490 was used to screen for mycoplasma once a month employing the LookOut® Mycoplasma PCR Detection
491 Kit (MP0035, Sigma-Aldrich) and JumpStart™ Taq DNA Polymerase (D9307, Sigma-Aldrich) to ensure
492 cells were free of mycoplasma contamination.
493

494 **Antibodies.** GAPDH (Cell Signaling Technology, 5174s, Rabbit antibody), MYCN (Santa Cruz
495 Biotechnology, 53993, Mouse antibody) , FLAG (Sigma, F1804, Mouse antibody), Biotin (Bethyl
496 Laboratories, A150-109A Rabbit), ACTIN (Sigma, A3854, mouse antibody), PUF60 (Thermo
497 Fisher, PA5-21411, Rabbit antibody), U2AF2 (Novus Biologicals, NBP2-04140, Rabbit antibody),
498 CPSF6 (Bethyl Laboratories, 357A,Rabbit antibody), DHX40 (Novus Biologicals, NBP1-91834,
499 Rabbit antibody), DHX8 (Abcam, AB181074, Rabbit antibody), LUC7L1 (Novus Biologicals,
500 NBP2-56401, Rabbit antibody), LUC7L2 (Novus Biologicals, NBP2-33621, Rabbit antibody), LUC7L3
501 (Novus Biologicals, NBP1-88053, Rabbit antibody), RBM39 (ATLAS, HPA001519, Rabbit antibody),
502 GLS (KGA-specific) (Proteintech,20170-1-AP, Rabbit antibody), GLS(GAC-Specific) (Proteintech,
503 19958-1-AP, Rabbit antibody), JMJD6 (ATLAS, HAP059156, Rabbit antibody), JMJD6 (Santa Cruz
504 biotechnology, sc-28348, Mouse antibody).
505
506 **Retroviral plasmids and retrovirus packaging.** MSCV-IRES-GFP and MSCV-IRES-mCherry were
507 obtained from St Jude Vector Core. Human JMJD6 and murine MYCN were subcloned into MSCV-IRES-
508 GFP and MSCV-IRES-mCherry, respectively. The MSCV-CMV-CMV-Flag-HA-JMJD6 was purchased
509 from Addgene (Addgene # plasmid 31358). The retrovirus packaging was done as described in the
510 following procedure. Briefly, HEK93T cells were transfected with viral vectors by combining 5µg of
511 target vector, 4.4µg of pMD-old-gag-pol, and 0.6µg of VSV-G plasmids in 400uL of DMEM without
512 serum or L-glutamine. PEIpro transfection reagent (Polyplus 115-010) was added at 2:1 (PEIpro µL: µg
513 of plasmid) per 100mm dish of cells and mixed well, and incubated at RT for at least 20 minutes, prior to
514 adding cells. The following day, fresh medium was added to cells. For 3-4 days, viral media was
515 harvested and replaced twice per day. Viral media was centrifuged at 1500RPM for 10 minutes and
516 filtered through a 0.45um vacuum filter. Virus was concentrated by ultracentrifugation at 28.5kRPM for
517 2 hours at 4C, aspirated, and resuspended in either OptiMEM or PBS, aliquoted, and frozen at -80C until
518 use. cDNAs for GAC and KGA were synthesized by GenScript and cloned into pGenLenti vector for
519 virus packaging.
520
521 **siRNA transfection**. 25uM of each siRNA oligo was resuspended in 500uL of prewarmed Opti-MEM,
522 reduced serum medium (Gibco Life technologies #31985-070) in 6 well plates. To each well, 7µL of
523 RNAiMax (Invitrogen Lipofectamine RNAiMAX transfection reagent 13778100) was added, mixed, and left
524 at room temperature for 10 minutes. After incubation, 100,000 cells of each indicated cell line were added
525 to each well in a total of 2mL volume with RPMI medium supplemented with 10% FBS. JMJD6 siRNA#63,
526 5-CCAAAGUUAUCAAGGAAA-3; JMJD6 siRNA#75, 5-CAGUGAAGAUGAAGAUGAA-3. U2AF2

527 siRNA#1 AGAAGAAGAAGGUCCGU; U2AF2 siRNA#2 GUGGCAGUUUCAUAUUUG. CPSF6
528 siRNA#1 GGAUCACCUUCCAAGACA. CPSF6 siRNA#2 AGAACCGUCAUGACGAUU. GLS1 siRNA,
529 CAACTGGCCAAATTCAGTC; GAC siRNA, CCTCTGTTCTGTCAGAGTT; KGA siRNA,
530 ACAGCGGGACTATGATTCT.
531
532 **SDS-PAGE and Western blot.** Cells were washed twice with ice-cold phosphate-buffered saline (PBS)
533 and directly lysed on ice with 2X sample loading buffer (0.1 M Tris HCl [pH 6.8], 200 mM dithiothreitol
534 [DTT], 0.01% bromophenol blue, 4% sodium dodecyl sulfate [SDS] and 20% glycerol). On ice, cell lysates
535 were sonicated once with a 5 second bursts at 40% amplitude output (Sonics, VIBRA CELL) followed by
536 25 minutes heating at 95 °C. After the cell lysates were centrifuged at 13,000 × g at room temperature for
537 2 mins, 10-20 µl of the cell lysates were separated on 4-15% Mini-PROTEAN® TGX™ Stain-Free™
538 Protein Gels from Bio-Rad and transferred to methanol-soaked polyvinylidene difluoride (PVDF)
539 membranes (Millipore). Lysates for RBM39 G268V mutant cell lines and DCAF15 genetically modified
540 cells were generated as previously described[107]. Membranes were blocked in PBS buffer supplemented
541 with 0.1% TWEEN 20 and 5% skim milk (PBS-T) and incubated for 1 hour at room temperature under
542 gentle horizontal shaking. Membranes were incubated overnight at 4 °C with the primary antibodies. The
543 next day, membranes were washed 3 times (for 5 minutes) with PBS-T at room temperature. Protected from
544 light, membranes were then incubated with goat anti-mouse or goat anti-rabbit HRP-conjugated secondary
545 antibodies (1:5,000) for 1 hour at room temperature, followed by three 5-minite washes with PBS-T at room
546 temperature. Lastly, membranes were incubated for 1 minute at room temperature with SuperSignal West
547 Pico PLUS Chemiluminescent Substrate (34580, Thermo Fisher Scientific) and the bound antigen-antibody
548 complexes were visualized using Odyssey Fc Imaging System (LI-COR Corp., Lincoln, NE).
549
550 **RNA extraction and RT-PCR isoforms of GLS.** RNA was extracted using RNeasy® Plus Mini Kit
551 (Qiagen, reference # 74136) following the manufacturer's protocol. cDNA was prepared in 20ul reaction
552 from 500ng of total RNA using Superscript™ IV First Strand Synthesis System (Invitrogen, reference #
553 1809105) kit. Real-time PCR reactions were run in triplicates (n=3) in the 7500 Real-time PCR system by
554 Applied Biosystems (Thermo Fisher Scientific) using power SYBR Green PCR master mix (Applied
555 Biosystems, reference # 4367660). ΔΔCT methods were applied to analyze the results. The following
556 primers were used to perform the quantitative Real-time PCR- GAPDH (Forward:
557 AACGGGAAGCTTGTCATCAATGGAAA, Reverse: GCATCAGCAGAGGGGGCAGAG), GAC
558 (Forward: GAGGTGCTGGCCAAAAAGCCT, Reverse: AGGCATTCGGTTGCCCAAACT), KGA
559 (Forward: CTGCAGAGGGTCATGTTGAA, Reverse: ATCCATGGGAGTGTTATTCCA).

560

561 **Lentiviral packaging of pLenti and shRNA.** The GAC and KGA cDNAs were synthesized by Genscript
562 company and cloned into pLenti vector. The TRC lentiviral-based shRNA knockdown plasmids for
563 JMJD6 were purchased from Horizon Discovery (sh#46: RHS3979-201781036,
564 TTAAACCAGGTAATAGCTTCG; sh#47: RHS3979-201781037, ATCTTCACTGAGTAGCCATCG)
565 The lentiviral shJMJD6 and shControl (pLKO.1) particles were packaged by Vector Lab at St Jude.
566 Briefly, HEK293T cells were transfected with shRNA constructs and helper plasmids (pCAG-kGP1-1R,
567 pCAG4-RTR2, and pHDM-G). The 48- and 72-hr post-transfection replication-incompetent lentiviral
568 particles were harvested and transduced into cells with 8μg/ml of polybrene. 48 hours later, 1 μg/ml of
569 puromycin was added for selection for additional 48 hours before injection into mice or immunoblotting.
570

571 **JMJD6 CRISPR KO method**. Genetically modified neuroblastoma cells were generated by using
572 CRISPR-Cas9 technology. Briefly, 400,000 NB cells were transiently co-transfected with 100pmol of
573 chemically modified gRNA (GGACTCTGGAGCGCCTAAAA) (Synthego), 33pmol of Cas9 protein (St.
574 Jude Protein Production Core), 200ng of pMaxGFP (Lonza), and, using solution P3 and program DS-150
575 in small cuvettes according to the manufacturer's recommended protocol. Five days post-nucleofection,
576 cells were sorted for GFP+ (transfected) cells and plated as single cells into 96-well plates. Cells were
577 clonally expanded and screened for the desired modification using targeted next generation sequencing
578 followed by analysis with CRIS.py (https://pubmed.ncbi.nlm.nih.gov/30862905/).
579

580 **Colony formation for JoMa1 cells**. Matrigel was kept at 4ºC to being liquified for 6 hours. 50μL of
581 Matrigel per 1 square centimeter area was added to 24-well plate without air bubbles. The 24-well plate
582 was kept at 37ºC in cell culture incubator till it was solidified. 200 of JoMa1 cells transduced with GFP,
583 JMJD6, MYCN, MYCN+JMJD6 in DMEM:F12 enriched media without tamoxifen were seeded onto the
584 24-well coated with Matrigel. This was done in triplicate. Cells were checked daily, and media were
585 changed every 3 days without disturbing the Matrigel by removing and adding media gently. To stain the
586 colonies, cells were fixed by formaldehyde (3.7% in PBS) for 2 min at room temperature, followed by
587 permeabilization with 100% methanol (not ice-cold) for 20min at room temperature. The colonies were
588 stained by 0.4% crystal violet.
589

590 **Crystal Violet Staining.** After removing media, cells were washed with Dulbecco's phosphate buffered
591 saline without calcium or magnesium (DPBS, Lonza) and treated with 4% formaldehyde in PBS (PFA)
592 for 20 minutes. Once PFA was removed, cells were stained with 0.1% crystal violet stain for 1 hour.

593 KGA/GAC overexpression colony formation: 5000 cells were plated of BE2C control, KGA and GAC
594 overexpressing cells and were culture for 7 days; 10,000 cells were plated of SKNAS control, KGA and
595 GAC overexpressing cells and were culture for 7 days (n=3). After 7 days, medium was removed and
596 cells were washed with Dulbecco's PBS (DPBS) (DPBS, Lonza) and treated with 4% formaldehyde in
597 PBS [paraformaldehyde (PFA)] for 30 min. PFA was later removed and cells were stained with 0.1%
598 crystal violet stain for 1 hour. Experiments were repeated twice. Indisulam treatment on WT and JMJD6-
599 KO cell lines: JMJD6-WT and KO cells were plated in 12-well plate (50,000 cells/well for SKNAS) and
600 6-well plate (5,000 cells/well for BE2C) (n=3). Next day, cells were treated with Indisulam with indicated
601 concentration for 7 days (SKNAS cells) and 5 days (BE2C cells). Crystal violet staining was performed
602 to visualize and quantify the colony formation. Experiments were repeated twice. Indisulam treatment on
603 KGA/GAC overexpressing cell lines: 10,000 BE2C and 100,000 SKNAS control, KGA and GAC
604 overexpressing cells were plated in 6-well plate (n=3). Next day, cells were treated with Indisulam for 7
605 days. Crystal violet staining was performed to visualize and quantify the colony formation. Experiments
606 were repeated twice.
607
608 **Click-iT AHA labeling assay for metabolic labeling of newly synthesized proteins**. Click-iT was
609 performed as previously described. Briefly, cells were plated at 5 million cells per 100mm dish in RPMI
610 supplemented with 10% FBS. Cells were washed with warm PBS and replaced with methionine-free
611 medium (Thermo 21013024 supplement with glutamine and sodium pyruvate) for 1 hour at 37° C in 5%
612 CO_2. Following, fresh methionine-free media containing 50µM of Click-iT AHA (L-azidohomoalanine)
613 (Thermo C10102) was added to the cells for 2 hours at 37°C. After AHA-labeling, cells were washed with
614 warm PBS and lysed with 1% SDS, 50mM Tris-HCl, (pH 8.0) supplemented with phosphatase inhibitors
615 (PhosSTOP, Sigma) and protease inhibitors (cOmplete mini, Roche) by applying the buffer directly to the
616 plate, incubating the cells on ice for 30 minutes, tilting the plates, and collecting the lysate. Lysates were
617 briefly sonicated, vortexed for 5 minutes, and centrifuged at 18,000xg for 5 minutes at 4°C. Total protein
618 quantification was assayed using the EZQ Protein Quantification Kit (Thermo R33200) according to the
619 manufacturer's protocol and results were read on a fluorescence-based microplate reader (BioTek Synergy
620 2). Click chemistry of the biotin-alkyne (PEG4 carboxamide-propargyl biotin) (Thermo B10185) to the
621 AHA-labeled lysates was performed using the Click-iT Protein Reaction Buffer Kit (Thermo C10276)
622 using a concentration of 40µM biotin-alkyne per click reaction (and no biotin-alkyne added for controls).
623 Following the click reaction, samples were either assayed for total biotinylated protein by following the
624 manufacturer's protocol. For total biotinylated protein, briefly, 600µL of methanol, 150µL of chloroform,
625 and 400µL of megaOhm water was sequentially added and vortexed, followed by centrifugation at

626 18,000xg for 5 minutes. The upper aqueous phase was discarded, and 450µL of methanol was added,
627 vortexed, and centrifuged again at 18,000xg for 5 minutes. This methanol step was performed in duplicate
628 to remove residual reaction components. Protein pellets were allowed to air dry and resuspended in a
629 suitable volume of sample buffer and heated prior to western blot analysis.
630
631 **Immunoprecipitation.** $5X10^6$ BE2C and SK-N-AS cells expressing Flag-JMJD6 were cultured in 150cm
632 dish with complete RPMI media. Cells were washed twice with cold PBS after reaching 95% confluency,
633 then lysed in 1ml lysis buffer (50mM Tris-HCl, pH 7.4, 150mM NaCl, 1mM EDTA, 1% Trion-X100 with
634 complete protease inhibitors (Sigma 11836170001, added fresh) and PhosSTOP (Sigma 4906845001).
635 Cells were scrapped into a 1.5mL Eppendorf tube and incubated on ice for 15min, which were mixed by
636 vortex every 5 min. Cell lysates were spun by 1,3500rpm for 10min at 4C. The supernatant was transferred
637 to a new tube. The cell lysates were subject to immunoprecipitation using M2 anti-Flag beads (Sigma,
638 M8823) overnight by rocking at 4ºC. The following day, beads were washed 3X with buffer and eluted
639 with 5 packed gel volumes of FLAG peptide in TBS buffer (3uL of stock FLAG peptide at 5ug/uL per
640 100uL of TBS buffer) while rotating at 4ºC for 30 minutes. Beads were briefly spun and the supernatant
641 was removed from the beads (eluate). This elution step was repeated one more time and pooled with the
642 first eluate. Prior to western blot, input, flow throughs, and elution samples were processed by adding 4X
643 sample buffer supplemented with 50mM DTT and heated at 75ºC for 10 minutes prior to running on a gel.
644
645 **RNA-immunoprecipitation.** SK-N-AS cells expressing Flag-JMJD6 were grown in a 10-cm dish in
646 RPMI complete media. After 70% confluency, cells were washed with cold PBS twice and then were
647 subject to lysis with Polysome Lysis Buffer (100mM KCl, 5mM $MgCl_2$, 10mM HEPES, pH7.0, 0.5% NP-
648 40, 1mM DTT, 100 U/ml RAasin RNase inhibitor (Promega, N2511), 2mM vanadyl ribonucleoside
649 complexes solution (Sigma, 94742), 25µL protease inhibitor cocktail for mammalian cells (Sigma,
650 P8340)). Cell lysates were precleared with magnetic IgG beads for 1 hour. The cell lysates were subject
651 to immunoprecipitation using M2 anti-Flag beads (Sigma, M8823) overnight by rocking at 4ºC. The same
652 amounts of lysates were saved at -80ºC for input RNA extraction. The beads were washed with 250 µL
653 Polysome Lysis Buffer for 4 times, flowed by washing with Polysome Lysis Buffer containing 1M urea.
654 RNA was released by adding 150µL of Polysome Lysis Buffer containing 0.1% SDS and 45µg proteinase
655 K (Ambion, AM2548) and incubated at 50ºC for 30min. RNA was extracted with phenol-chloroform-
656 isoamyl alcohol mixture (Sigma, 77618). RNA was recovered by adding 2µL of GlycoBlue (15mg/ml,
657 Ambion, AM9516), 36µL of 3M sodium acetate and 750µL ethanol followed by incubation at -20ºC for
658 overnight. RNA was precipitated with 70% ethanol and air dried, followed by resuspension with RNase-

659 free water followed by DNaseI (Promega, M6101) treatment to remove genomic DNA. The resultant
660 RNAs were subjected to RT-qPCR analysis using 3 sets of GAC and KGA primers and 18S rRNA as
661 control. 18S rRNA F: GCTTAATTTGACTCAACACGGGA; 18S rRNA R:
662 AGCTATCAATCTGTCAATCCTGTC. GLS-GACiso_F: GAGGTGCTGGCCAAAAAGCCT; GLS-
663 GACiso_R: AGGCATTCGGTTGCCCAAACT. GLS-KGAiso_F: CTGCAGAGGGTCATGTTGAA;
664 GLS-KGAiso_R: ATCCATGGGAGTGTTATTCCA. KGA_set2_F:
665 GCAGCCTCCAGGTGCTTTCA; KGA_set2_R: GTAATGGGAGGGCAGTGGCA. KGA_set3_F:
666 TGCCCGACACTGCCCTTTAG; KGA_set3_R: CCTGCCAGACAGACAACAGCA. GAC_set2_F:
667 TGCTTCTCAAGGCCTTACTGC; GAC_set2_R: AGGCATTCGGTTGCCCAAACT. GAC_set3_F:
668 CCTTCTAGAGGTGCTGGCCAAA; GAC_set3_R: TGCAACACAAATATGCAGTAAGGC. For
669 validation of protein immunoprecipitation, 20% of beads after overnight incubation were removed and
670 processed as follows: Beads were washed 3X with buffer and eluted with 5 packed gel volumes of FLAG
671 peptide in TBS buffer (3μL of stock FLAG peptide at 5μg/μL per 100uL of TBS buffer) while rotating at
672 4ºC for 30 minutes. Beads were briefly spun and the supernatant was removed from the beads (eluate).
673 This elution step was repeated one more time and pooled with the first eluate.
674
675 **Identification of JMJD6 interacting partners by LC-MS/MS**. Protein samples were run on a short gel
676 as described in a previously published protocol[108]. Proteins in the gel bands were reduced with
677 dithiothreitol (DTT) (Sigma) and alkylated by iodoacetamide (IAA) (Sigma). The gel bands were then
678 washed, dried, and rehydrated with a buffer containing trypsin (Promega). Samples were digested
679 overnight, acidified and the resulting peptides were extracted. The extracts were dried and reconstituted
680 in 5% formic acid. The peptide samples were loaded on a nanoscale capillary reverse phase C18 column
681 by a HPLC system (Thermo EASY-nLC 1000) and eluted by a gradient. The eluted peptides were ionized
682 and detected by a mass spectrometer (Thermo LTQ Orbitrap Elite). The MS and MS/MS spectra were
683 collected over a 90-min liquid chromatography gradient. Database searches were performed using Sequest
684 (version 28 revision 13) search engine against a composite target / decoy Uniprot human protein database.
685 All matched MS/MS spectra were filtered by mass accuracy and matching scores to reduce protein false
686 discovery rate to <1%. Spectral counts, matching to individual proteins reflect their relative abundance in
687 one sample after the protein size is normalized. The spectral counts between samples for a given protein
688 was used to calculate the p-value based on G-test [109].
689
690 **Metabolome profiling by LC-MS/MS**. JMJD6 knockout or parental SK-N-AS cells were cultured in 6-
691 well plates to ~85% confluence and washed with 2 mL ice cold 1X Phosphate-Buffered Saline (PBS). The

692 cells were then harvested in 300 µL freezing 80% acetonitrile (v/v) into 1.5 mL tubes and lysed in the
693 presence of 0.5mm Zirconia/silica beads by Bullet Blender (Next Advance) at 4 °C until the sample were
694 homogenized. The resulting lysate was then centrifuged at 21,000 x g for 5 min and the supernatant was
695 dried by speedvac. The samples were resuspended in 50 µL of 1% acetonitrile plus 0.1% trifluoroacetic
696 acid, and separated by Ultra-C18 Micro spin columns (Harvard apparatus) into hydrophilic metabolites
697 (flow through) and hydrophobic metabolites (eluent of 125 µL of 80% acetonitrile plus 0.1%
698 trifluoroacetic acid). Ten µL of hydrophilic metabolites were dried, reconstituted in 3 µL of 66%
699 acetonitrile and analyzed by a ZIC-HILIC column (150 × 2.1 mm, EMD Millipore) coupled with a Q
700 Exactive HF Orbitrap MS (Thermo Fisher) in negative mode and metabolites were eluted within a 45 min
701 gradient (buffer A: 10mM ammonium acetate in 90% acetonitrile (pH=8); buffer B: 10mM ammonium
702 acetate in 100% H_2O (pH=8)). Twenty µL of hydrophobic metabolites were dried and resuspend in 3 µL
703 of 5% formic acid followed by separation with a self-packed nanoC18 column (75 µm × 15 cm with 1.9
704 µm C18 resin from Dr. Maisch GmbH) and detection with a Q Exactive HF Orbitrap MS (Thermo Fisher)
705 in positive mode. Metabolites were eluted within a 50 min gradient (buffer A: 0.2% formic acid in H_2O;
706 buffer B: 0.2% formic acid in acetonitrile). MS settings for both types of samples included MS1 scans
707 (120,000 resolution, 100-1000 *m/z*, 3 x 10^6 AGC and 50 ms maximal ion time) and 20 data-dependent
708 MS2 scans (30,000 resolution, 2 x 10^5 AGC, ~45 ms maximal ion time, HCD, Stepped NCE (50, 100,
709 150), and 20 s dynamic exclusion). A mix of all samples served as quality control was injected in the
710 beginning, middle and the end of the samples to monitor the signal stability of the instrument. The data
711 analysis was performed by a recently developed software suite JUMPm. Raw files were converted to
712 mzXML format followed by peak feature detection for individual sample and feature alignment across
713 samples. Metabolite identification was supported by matching the retention time, accurate mass/charge
714 (m/z) ratio, and MS/MS fragmentation data to our in-house authentic compound library and the matching
715 of m/z and MS/MS fragmentation data to, downloaded experimental MS/MS library (MoNA,
716 https://mona.fiehnlab.ucdavis.edu/), in-silico database generated from Human Metabolome Database
717 (HMDB), and mzCloud (https://mzcloud.org). Peak intensities were used for metabolite quantification.
718 The data was normalized by both cell numbers (before data collection) and trimmed median intensity of
719 all features across samples (post data collection).
720
721 **Differential gene expression and gene set enrichment analysis (GSEA) for RNA-seq experiments.**
722 Total RNA from cells and tumor tissues were performed using the RNeasy Mini Kit (Qiagen) according
723 to the manufacturer's instructions. Paired-end sequencing was performed using the High-Seq platform
724 with 100bp read length. Total stranded RNA sequencing data were processed by the internal AutoMapper

725 pipeline. Briefly the raw reads were firs trimmed (Trim-Galore version 0.60), mapped to human genome
726 assembly (GRCh38) (STAR v2.7) and then the gene level values were quantified (RSEM v1.31) based on
727 GENCODE annotation (v31). Low count genes were removed from analysis using a CPM cutoff
728 corresponding to a count of 10 reads and only confidently annotated (level 1 and 2 gene annotation) and
729 protein-coding genes are used for differential expression analysis. Normalization factors were generated
730 using the TMM method, counts were then transformed using voom and transformed counts were analyzed
731 using the lmFit and eBayes functions (R limma package version 3.42.2). The significantly up- and down-
732 regulated genes were defined by at least 2-fold changes and adjusted p-value < 0.05. Then gene set
733 enrichment analysis (GSEA) was carried out using gene-level log2 fold changes from differential
734 expression results against gene sets in the Molecular Signatures Database (MSigDB 6.2) (gsea2 version
735 2.2.3).
736
737 **RNA splicing analysis.** After mapping RNA-seq data, rMATS v4.1.0 was used for RNA alternative
738 splicing analysis by using the mapped BAM files as input. Specifically, five different kinds of alternative
739 splicing events were identified, i.e., skipped exon (SE), alternative 5'-splicing site (A5SS), alternative 3'-
740 splicing site (A3SS), mutually exclusive exon (MXE) and intron retention (RI). To keep consistent, the
741 same GTF annotation reference file for mapping was used for rMATS. For stranded RNA-seq data, the
742 argument "--libType fr-firststrand" was applied. To process reads with variable lengths, the argument "--
743 variable-read-length" was also used for rMATS. To select statistically significantly differential splicing
744 events, the following thresholds were used: FDR <0.05 and the absolute value of IncLevelDifference >
745 0.1. For visualization, the IGV Genome Browser was used to show the sashimi plots of splicing events.
746 To investigate the genome-wide correlations of differential splicing between two genotypes (e.g., shRNA
747 knockdown of JMJD6 and non-target shRNA in cells), we extracted splice junctions for all samples of
748 both genotypes of interest from the STAR[110] output files suffixed with "SJ.out.tab", which contain high
749 confidence collapsed splice junctions. Only those unique mapped reads crossing the junctions were
750 considered. By extracting the union of the unique junction positions, we constructed a unified junction-
751 read feature vector for each sample. Then, we normalized the junction-read vectors of each sample with
752 TMM method in "voom" and "limma" and R package, assuming a negative binomial distribution. Next,
753 we averaged the junction-read vectors for samples of the same genotype. The gene level expression was
754 estimated based on the canonical junctions from the most abundant isoforms estimated for each gene. The
755 fold changes of exon junctions significantly deviated from gene level changes were regarded as
756 differentially spliced junctions for between cell-line comparisons.
757

758 **Data mining**. *JMJD6, GAC and KGA* expression in tumor tissues were downloaded from R2
759 (https://portals.broadinstitute.org/ccle), Kocak dataset GSE45547 (649 samples) and Fischer dataset
760 GSE120572 (394 samples). In both datasets, the probe UKv4_A_23_P311616 represented *JMJD6*, the
761 probe UKv4_A_23_P308800 represented *GAC* and UKv4_A_23_P39766 represented *KGA*. *JMJD6*
762 expression data from the RNA-seq data of various pediatric cancer tissues were downloaded from St Jude
763 cloud (https://pecan.stjude.cloud/). The copy number alterations of *JMJD6* and the related Kaplan-Meier
764 analysis were downloaded from cBioportal (cbioportal.org). The data for correlation of metabolite
765 abundance and JMJD6 knockout effect were downloaded from DepMap (https://depmap.org/portal/).
766
767 **Pathway network analysis**. The 114 essential fitness genes to neuroblastoma cell survival identified
768 through genome-wide CRISPR/Cas9 library screen were uploaded into STRING program (https://string-
769 db.org) for network interaction analysis with confidence threshold 0.15. The resulting network was then
770 uploaded into Cytoscape program for presentation[111]. The clusters were grouped based on the biological
771 functions of each gene.
772
773 **Copy number analysis of JMJD6 and other genes encoding JmjC domain histone demethylases from**
774 **St Jude neuroblastoma cohort.** Somatic copy number alternations (SCNA) were determined by
775 CONSERTING (PMID: 25938371) for each pair of tumor and normal samples. The normalize read depth
776 ratio (log2 ratio) for the CNV segments with JmjC-domain containing proteins were extracted and used
777 for CNV heatmap generation (https://CRAN. R-project. org/package= pheatmap) and hierarchical
778 clustering of samples.
779
780 **Xenograft studies.** (**1**) shRNA-mediated JMJD6 knockdown. Neuroblastoma cells were transduced with
781 shRNA lentiviral particles targeting JMJD6. 48 hours later, 1 μg/ml of puromycin was added for selection
782 for additional 48 hours. Cancer cells ($5x10^6$) were mixed with Matrigel (1:1 ratio in volume) and
783 subcutaneously injected into the flank sites of NSG mice. (**2**) JMJD6 and MYC-mediated transformation.
784 After JoMa1 cells were transduced with GFP, JMJD6, MYCN and JMJD6/MYCN, 10^4 cells per group
785 were mixed with Matrigel (1:1 ratio in volume) and subcutaneously injected into the flank sites of NSG
786 mice. Mice were sacrificed when they reached the humane endpoint. Tumors were measured by using
787 electronic calipers, and volumes calculated as width π/6 xd3 where d is the mean of two diameters taken
788 at right angles.
789

Statistical analysis. All quantitative data are presented as mean ± SD. Unpaired Student's t test was performed for comparison of two groups. Spearman correlation was used to assess the relationship between two variables. Kaplan-Meier method was used to estimate the survival rate. Mann-Whitney rank test (two-sided) was used to compare the tumor volume between two groups at every time point. P-values across multiple time points were adjusted for multiple comparison using the Holm-SidaK method. $p<0.05$ was considered as statistically significant. All the statistical analyses, except where otherwise noted, were performed using GraphPad Prism (v9).

Data accessibility. GEO accession number: GSE185867

To review GEO accession GSE185867: Go to https://nam11.safelinks.protection.outlook.com/?url=https%3A%2F%2Fwww.ncbi.nlm.nih.gov%2Fgeo%2Fquery%2Facc.cgi%3Facc%3DGSE185867&data=04%7C01%7Cjun.yang2%40stjude.org%7C56d8ac619531468173d608d98ea927d8%7C22340fa892264871b677d3b3e377af72%7C0%7C0%7C637697679446209542%7CUnknown%7CTWFpbGZsb3d8eyJWIjoiMC4wLjAwMDAiLCJQIjoiV2luMzIiLCJBTiI6Ik1haWwiLCJXVCI6Mn0%3D%7C1000&sdata=XtZl1ttoOPBvfhwmX9uCcwVN1Yg02qDsvcsHdJv58xw%3D&reserved=0

Enter token qzixwsoohbsxjij into the box

Acknowledgements. We thank the staff of the St. Jude Animal Resource Center and Hartwell Center for their dedication and expertise. We thank COG for providing cell lines. The work was supported by American Cancer Society-Research Scholar (130421-RSG-17-071-01-TBG, J.Y.), National Cancer Institute (1R01CA229739-01, J.Y., R01CA266600, J.Y.). The work was also supported by the American Lebanese Syrian Associated Charities (ALSAC). The content is solely the responsibility of the authors and does not necessarily represent the official views of the National Institutes of Health.

Author contributions. C.J., W.Q., S.S., H.H., D.H.B. D.H performed experiments. G.W., H.J., T-C.C., D.F., J-H.C performed proteomic, genomic and RNA-seq analysis. S.M.S and S.M.P-M provided CRISPR knockout. R.W., K.F. provided key reagents. A.M.D, A.M., J.P., and J.Y. supervised the studies. J.Y conceived the project and wrote the manuscript with help from co-authors.

References

1 Hanahan, D. & Weinberg, R. A. Hallmarks of cancer: the next generation. *Cell* **144**, 646-674 (2011). https://doi.org:10.1016/j.cell.2011.02.013

2 Pavlova, N. N. & Thompson, C. B. The Emerging Hallmarks of Cancer Metabolism. *Cell Metab* **23**, 27-47 (2016). https://doi.org:10.1016/j.cmet.2015.12.006

3 Vazquez, A. *et al.* Cancer metabolism at a glance. *J Cell Sci* **129**, 3367-3373 (2016). https://doi.org:10.1242/jcs.181016

4 DeBerardinis, R. J. & Chandel, N. S. Fundamentals of cancer metabolism. *Sci Adv* **2**, e1600200 (2016). https://doi.org:10.1126/sciadv.1600200

5 Kalkat, M. *et al.* MYC Deregulation in Primary Human Cancers. *Genes (Basel)* **8** (2017). https://doi.org:10.3390/genes8060151

6 Stine, Z. E., Walton, Z. E., Altman, B. J., Hsieh, A. L. & Dang, C. V. MYC, Metabolism, and Cancer. *Cancer Discov* **5**, 1024-1039 (2015). https://doi.org:10.1158/2159-8290.CD-15-0507

7 Hsu, T. Y. *et al.* The spliceosome is a therapeutic vulnerability in MYC-driven cancer. *Nature* **525**, 384-388 (2015). https://doi.org:10.1038/nature14985

8 Hirsch, C. L. *et al.* Myc and SAGA rewire an alternative splicing network during early somatic cell reprogramming. *Genes Dev* **29**, 803-816 (2015). https://doi.org:10.1101/gad.255109.114

9 Koh, C. M. *et al.* MYC regulates the core pre-mRNA splicing machinery as an essential step in lymphomagenesis. *Nature* **523**, 96-100 (2015). https://doi.org:10.1038/nature14351

10 Phillips, J. W. *et al.* Pathway-guided analysis identifies Myc-dependent alternative pre-mRNA splicing in aggressive prostate cancers. *Proc Natl Acad Sci U S A* **117**, 5269-5279 (2020). https://doi.org:10.1073/pnas.1915975117

11 Anczukow, O. & Krainer, A. R. The spliceosome, a potential Achilles heel of MYC-driven tumors. *Genome Med* **7**, 107 (2015). https://doi.org:10.1186/s13073-015-0234-3

12 Zhang, S. *et al.* MYCN controls an alternative RNA splicing program in high-risk metastatic neuroblastoma. *Cancer Lett* **371**, 214-224 (2016). https://doi.org:10.1016/j.canlet.2015.11.045

13 Gustafson, W. C. & Weiss, W. A. Myc proteins as therapeutic targets. *Oncogene* **29**, 1249-1259 (2010). https://doi.org:10.1038/onc.2009.512

14 Weiss, W. A., Aldape, K., Mohapatra, G., Feuerstein, B. G. & Bishop, J. M. Targeted expression of MYCN causes neuroblastoma in transgenic mice. *EMBO J* **16**, 2985-2995 (1997). https://doi.org:10.1093/emboj/16.11.2985

15 Zhu, S. *et al.* Activated ALK collaborates with MYCN in neuroblastoma pathogenesis. *Cancer Cell* **21**, 362-373 (2012). https://doi.org:10.1016/j.ccr.2012.02.010

16 Tao, L. *et al.* MYCN-driven fatty acid uptake is a metabolic vulnerability in neuroblastoma. *Nat Commun* **13**, 3728 (2022). https://doi.org:10.1038/s41467-022-31331-2

17 Khan, A. *et al.* Targeting metabolic activity in high-risk neuroblastoma through Monocarboxylate Transporter 1 (MCT1) inhibition. *Oncogene* **39**, 3555-3570 (2020). https://doi.org:10.1038/s41388-020-1235-2

18 Gamble, L. D. *et al.* Inhibition of polyamine synthesis and uptake reduces tumor progression and prolongs survival in mouse models of neuroblastoma. *Sci Transl Med* **11** (2019). https://doi.org:10.1126/scitranslmed.aau1099

19 Xia, Y. *et al.* Metabolic Reprogramming by MYCN Confers Dependence on the Serine-Glycine-One-Carbon Biosynthetic Pathway. *Cancer Res* **79**, 3837-3850 (2019). https://doi.org:10.1158/0008-5472.CAN-18-3541

20 Wang, T. *et al.* MYCN drives glutaminolysis in neuroblastoma and confers sensitivity to an ROS augmenting agent. *Cell Death Dis* **9**, 220 (2018). https://doi.org:10.1038/s41419-018-0295-5

21 Bansal, M., Gupta, A. & Ding, H. F. MYCN and Metabolic Reprogramming in Neuroblastoma. *Cancers (Basel)* **14** (2022). https://doi.org:10.3390/cancers14174113

22 Olsen, T. K. *et al.* DHODH is an independent prognostic marker and potent therapeutic target in neuroblastoma. *JCI Insight* **7** (2022). https://doi.org:10.1172/jci.insight.153836

23 Alborzinia, H. *et al.* MYCN mediates cysteine addiction and sensitizes neuroblastoma to ferroptosis. *Nat Cancer* **3**, 471-485 (2022). https://doi.org:10.1038/s43018-022-00355-4

24 Guo, X., Chen, Q. R., Song, Y. K., Wei, J. S. & Khan, J. Exon array analysis reveals neuroblastoma tumors have distinct alternative splicing patterns according to stage and MYCN amplification status. *BMC Med Genomics* **4**, 35 (2011). https://doi.org:10.1186/1755-8794-4-35

25 Shi, Y. *et al.* Aberrant splicing in neuroblastoma generates RNA-fusion transcripts and provides vulnerability to spliceosome inhibitors. *Nucleic Acids Res* (2021). https://doi.org:10.1093/nar/gkab054

26 Shi, Y. *et al.* Aberrant splicing in neuroblastoma generates RNA-fusion transcripts and provides vulnerability to spliceosome inhibitors. *Nucleic Acids Res* **49**, 2509-2521 (2021). https://doi.org:10.1093/nar/gkab054

27 Singh, S. *et al.* Targeting the spliceosome through RBM39 degradation results in exceptional responses in high-risk neuroblastoma models. *Sci Adv* **7**, eabj5405 (2021). https://doi.org:10.1126/sciadv.abj5405

28 Nijhuis, A. *et al.* Indisulam targets RNA splicing and metabolism to serve as a therapeutic strategy for high-risk neuroblastoma. *Nat Commun* **13**, 1380 (2022). https://doi.org:10.1038/s41467-022-28907-3

29 Pugh, T. J. *et al.* The genetic landscape of high-risk neuroblastoma. *Nat Genet* **45**, 279-284 (2013). https://doi.org:10.1038/ng.2529

30 Molenaar, J. J. *et al.* Sequencing of neuroblastoma identifies chromothripsis and defects in neuritogenesis genes. *Nature* **483**, 589-593 (2012). https://doi.org:10.1038/nature10910

31 Hagenbuchner, J., Kiechl-Kohlendorfer, U., Obexer, P. & Ausserlechner, M. J. BIRC5/Survivin as a target for glycolysis inhibition in high-stage neuroblastoma. *Oncogene* **35**, 2052-2061 (2016). https://doi.org:10.1038/onc.2015.264

32 MacArthur, I. C. *et al.* Prohibitin promotes de-differentiation and is a potential therapeutic target in neuroblastoma. *JCI Insight* **5** (2019). https://doi.org:10.1172/jci.insight.127130

33 Milosevic, J. *et al.* PPM1D Is a Therapeutic Target in Childhood Neural Tumors. *Cancers (Basel)* **13** (2021). https://doi.org:10.3390/cancers13236042

34 Meitinger, F. *et al.* TRIM37 controls cancer-specific vulnerability to PLK4 inhibition. *Nature* **585**, 440-446 (2020). https://doi.org:10.1038/s41586-020-2710-1

35 Garcia-Lopez, J. *et al.* Large 1p36 Deletions Affecting Arid1a Locus Facilitate Mycn-Driven Oncogenesis in Neuroblastoma. *Cell Rep* **30**, 454-464 e455 (2020). https://doi.org:10.1016/j.celrep.2019.12.048

36 Henrich, K. O. *et al.* CAMTA1, a 1p36 tumor suppressor candidate, inhibits growth and activates differentiation programs in neuroblastoma cells. *Cancer Res* **71**, 3142-3151 (2011). https://doi.org:10.1158/0008-5472.CAN-10-3014

37 Liu, Z. *et al.* CASZ1, a candidate tumor-suppressor gene, suppresses neuroblastoma tumor growth through reprogramming gene expression. *Cell Death Differ* **18**, 1174-1183 (2011). https://doi.org:10.1038/cdd.2010.187

38 Laut, A. K. *et al.* CHD5 inhibits metastasis of neuroblastoma. *Oncogene* **41**, 622-633 (2022). https://doi.org:10.1038/s41388-021-02081-0

39 Higashi, M. *et al.* Retinoic acid-induced CHD5 upregulation and neuronal differentiation of neuroblastoma. *Mol Cancer* **14**, 150 (2015). https://doi.org:10.1186/s12943-015-0425-y

40 Fujita, T. *et al.* CHD5, a tumor suppressor gene deleted from 1p36.31 in neuroblastomas. *J Natl Cancer Inst* **100**, 940-949 (2008). https://doi.org:10.1093/jnci/djn176

41 Fell, S. M. *et al.* Neuroblast differentiation during development and in neuroblastoma requires KIF1Bbeta-mediated transport of TRKA. *Genes Dev* **31**, 1036-1053 (2017). https://doi.org:10.1101/gad.297077.117

42 Li, S. *et al.* The 1p36 Tumor Suppressor KIF 1Bbeta Is Required for Calcineurin Activation, Controlling Mitochondrial Fission and Apoptosis. *Dev Cell* **36**, 164-178 (2016). https://doi.org:10.1016/j.devcel.2015.12.029

43 Chen, Z. X. *et al.* RNA helicase A is a downstream mediator of KIF1Bbeta tumor-suppressor function in neuroblastoma. *Cancer Discov* **4**, 434-451 (2014). https://doi.org:10.1158/2159-8290.CD-13-0362

44 Cole, K. A. *et al.* A functional screen identifies miR-34a as a candidate neuroblastoma tumor suppressor gene. *Mol Cancer Res* **6**, 735-742 (2008). https://doi.org:10.1158/1541-7786.MCR-07-2102

45 Yu, F. *et al.* RUNX3 interacts with MYCN and facilitates protein degradation in neuroblastoma. *Oncogene* **33**, 2601-2609 (2014). https://doi.org:10.1038/onc.2013.221

46 Bown, N. *et al.* Gain of chromosome arm 17q and adverse outcome in patients with neuroblastoma. *N Engl J Med* **340**, 1954-1961 (1999). https://doi.org:10.1056/NEJM199906243402504

47 Althoff, K. *et al.* A Cre-conditional MYCN-driven neuroblastoma mouse model as an improved tool for preclinical studies. *Oncogene* **34**, 3357-3368 (2015). https://doi.org:10.1038/onc.2014.269

48 Bottger, A., Islam, M. S., Chowdhury, R., Schofield, C. J. & Wolf, A. The oxygenase Jmjd6--a case study in conflicting assignments. *Biochem J* **468**, 191-202 (2015). https://doi.org:10.1042/BJ20150278

49 Chang, B., Chen, Y., Zhao, Y. & Bruick, R. K. JMJD6 is a histone arginine demethylase. *Science* **318**, 444-447 (2007). https://doi.org:10.1126/science.1145801

50 Webby, C. J. *et al.* Jmjd6 catalyses lysyl-hydroxylation of U2AF65, a protein associated with RNA splicing. *Science* **325**, 90-93 (2009). https://doi.org:10.1126/science.1175865

51 Kwok, J., O'Shea, M., Hume, D. A. & Lengeling, A. Jmjd6, a JmjC Dioxygenase with Many Interaction Partners and Pleiotropic Functions. *Front Genet* **8**, 32 (2017). https://doi.org:10.3389/fgene.2017.00032

52 Vangimalla, S. S., Ganesan, M., Kharbanda, K. K. & Osna, N. A. Bifunctional Enzyme JMJD6 Contributes to Multiple Disease Pathogenesis: New Twist on the Old Story. *Biomolecules* **7** (2017). https://doi.org:10.3390/biom7020041

53 Zhou, J. *et al.* An oncogenic JMJD6-DGAT1 axis tunes the epigenetic regulation of lipid droplet formation in clear cell renal cell carcinoma. *Mol Cell* **82**, 3030-3044 e3038 (2022). https://doi.org:10.1016/j.molcel.2022.06.003

54 Paschalis, A. *et al.* JMJD6 Is a Druggable Oxygenase That Regulates AR-V7 Expression in Prostate Cancer. *Cancer Res* **81**, 1087-1100 (2021). https://doi.org:10.1158/0008-5472.CAN-20-1807

55 Yang, J. *et al.* Targeting Histone Demethylases in MYC-Driven Neuroblastomas with Ciclopirox. *Cancer Res* **77**, 4626-4638 (2017). https://doi.org:10.1158/0008-5472.CAN-16-0826

56 Wong, M. *et al.* JMJD6 is a tumorigenic factor and therapeutic target in neuroblastoma. *Nat Commun* **10**, 3319 (2019). https://doi.org:10.1038/s41467-019-11132-w

57 Liu, W. *et al.* Brd4 and JMJD6-associated anti-pause enhancers in regulation of transcriptional pause release. *Cell* **155**, 1581-1595 (2013). https://doi.org:10.1016/j.cell.2013.10.056

58 Miller, T. E. *et al.* Transcription elongation factors represent in vivo cancer dependencies in glioblastoma. *Nature* **547**, 355-359 (2017). https://doi.org:10.1038/nature23000

59 Loven, J. *et al.* Selective inhibition of tumor oncogenes by disruption of super-enhancers. *Cell* **153**, 320-334 (2013). https://doi.org:10.1016/j.cell.2013.03.036

60 Chapuy, B. *et al.* Discovery and characterization of super-enhancer-associated dependencies in diffuse large B cell lymphoma. *Cancer Cell* **24**, 777-790 (2013). https://doi.org:10.1016/j.ccr.2013.11.003

61 Puissant, A. *et al.* Targeting MYCN in neuroblastoma by BET bromodomain inhibition. *Cancer Discov* **3**, 308-323 (2013). https://doi.org:10.1158/2159-8290.CD-12-0418

62 Wyce, A. *et al.* BET inhibition silences expression of MYCN and BCL2 and induces cytotoxicity in neuroblastoma tumor models. *PLoS One* **8**, e72967 (2013). https://doi.org:10.1371/journal.pone.0072967

63 Meyers, R. M. *et al.* Computational correction of copy number effect improves specificity of CRISPR-Cas9 essentiality screens in cancer cells. *Nat Genet* **49**, 1779-1784 (2017). https://doi.org:10.1038/ng.3984

64 Morgenstern, D. A. *et al.* The challenge of defining "ultra-high-risk" neuroblastoma. *Pediatr Blood Cancer* **66**, e27556 (2019). https://doi.org:10.1002/pbc.27556

65 Cerami, E. *et al.* The cBio cancer genomics portal: an open platform for exploring multidimensional cancer genomics data. *Cancer Discov* **2**, 401-404 (2012). https://doi.org:10.1158/2159-8290.CD-12-0095

66 Brodeur, G. M. & Bagatell, R. Mechanisms of neuroblastoma regression. *Nat Rev Clin Oncol* **11**, 704-713 (2014). https://doi.org:10.1038/nrclinonc.2014.168

67 Kameneva, P. *et al.* Single-cell transcriptomics of human embryos identifies multiple sympathoblast lineages with potential implications for neuroblastoma origin. *Nat Genet* **53**, 694-706 (2021). https://doi.org:10.1038/s41588-021-00818-x

68 Jansky, S. *et al.* Single-cell transcriptomic analyses provide insights into the developmental origins of neuroblastoma. *Nat Genet* **53**, 683-693 (2021). https://doi.org:10.1038/s41588-021-00806-1

69 Maurer, J. *et al.* Establishment and controlled differentiation of neural crest stem cell lines using conditional transgenesis. *Differentiation* **75**, 580-591 (2007). https://doi.org:10.1111/j.1432-0436.2007.00164.x

70 Delmore, J. E. *et al.* BET bromodomain inhibition as a therapeutic strategy to target c-Myc. *Cell* **146**, 904-917 (2011). https://doi.org:10.1016/j.cell.2011.08.017

71 Liu, W. *et al.* Brd4 and JMJD6-associated anti-pause enhancers in regulation of transcriptional pause release. *Cell* **155**, 1581-1595 (2013). https://doi.org:10.1016/j.cell.2013.10.056

72 Wu, G. *et al.* Inhibition of SF3B1 by molecules targeting the spliceosome results in massive aberrant exon skipping. *RNA* **24**, 1056-1066 (2018). https://doi.org:10.1261/rna.065383.117

73 Dang, C. V. MYC, metabolism, cell growth, and tumorigenesis. *Cold Spring Harb Perspect Med* **3** (2013). https://doi.org:10.1101/cshperspect.a014217

74 Miller, D. M., Thomas, S. D., Islam, A., Muench, D. & Sedoris, K. c-Myc and cancer metabolism. *Clin Cancer Res* **18**, 5546-5553 (2012). https://doi.org:10.1158/1078-0432.CCR-12-0977

75 Gordan, J. D., Thompson, C. B. & Simon, M. C. HIF and c-Myc: sibling rivals for control of cancer cell metabolism and proliferation. *Cancer Cell* **12**, 108-113 (2007). https://doi.org:10.1016/j.ccr.2007.07.006

76 Wise, D. R. & Thompson, C. B. Glutamine addiction: a new therapeutic target in cancer. *Trends Biochem Sci* **35**, 427-433 (2010). https://doi.org:10.1016/j.tibs.2010.05.003

77 Porter, L. D., Ibrahim, H., Taylor, L. & Curthoys, N. P. Complexity and species variation of the kidney-type glutaminase gene. *Physiol Genomics* **9**, 157-166 (2002). https://doi.org:10.1152/physiolgenomics.00017.2002

78 Cassago, A. *et al.* Mitochondrial localization and structure-based phosphate activation mechanism of Glutaminase C with implications for cancer metabolism. *Proc Natl Acad Sci U S A* **109**, 1092-1097 (2012). https://doi.org:10.1073/pnas.1112495109

79 Wang, J. B. *et al.* Targeting mitochondrial glutaminase activity inhibits oncogenic transformation. *Cancer Cell* **18**, 207-219 (2010). https://doi.org:10.1016/j.ccr.2010.08.009

80 Gao, P. *et al.* c-Myc suppression of miR-23a/b enhances mitochondrial glutaminase expression and glutamine metabolism. *Nature* **458**, 762-765 (2009). https://doi.org:10.1038/nature07823

81 Wise, D. R. *et al.* Myc regulates a transcriptional program that stimulates mitochondrial glutaminolysis and leads to glutamine addiction. *Proc Natl Acad Sci U S A* **105**, 18782-18787 (2008). https://doi.org:10.1073/pnas.0810199105

82 Yuneva, M., Zamboni, N., Oefner, P., Sachidanandam, R. & Lazebnik, Y. Deficiency in glutamine but not glucose induces MYC-dependent apoptosis in human cells. *J Cell Biol* **178**, 93-105 (2007). https://doi.org:10.1083/jcb.200703099

1019 83 Masamha, C. P. *et al.* CFIm25 regulates glutaminase alternative terminal exon definition to
1020 modulate miR-23 function. *RNA* **22**, 830-838 (2016). https://doi.org:10.1261/rna.055939.116
1021 84 Yi, J. *et al.* JMJD6 and U2AF65 co-regulate alternative splicing in both JMJD6 enzymatic activity
1022 dependent and independent manner. *Nucleic Acids Res* **45**, 3503-3518 (2017).
1023 https://doi.org:10.1093/nar/gkw1144
1024 85 Li, H. *et al.* The landscape of cancer cell line metabolism. *Nat Med* **25**, 850-860 (2019).
1025 https://doi.org:10.1038/s41591-019-0404-8
1026 86 David, C. J., Chen, M., Assanah, M., Canoll, P. & Manley, J. L. HnRNP proteins controlled by c-
1027 Myc deregulate pyruvate kinase mRNA splicing in cancer. *Nature* **463**, 364-368 (2010).
1028 https://doi.org:10.1038/nature08697
1029 87 Rauch, J. *et al.* c-Myc regulates RNA splicing of the A-Raf kinase and its activation of the ERK
1030 pathway. *Cancer Res* **71**, 4664-4674 (2011). https://doi.org:10.1158/0008-5472.CAN-10-4447
1031 88 Ge, Y. *et al.* The splicing factor RBM25 controls MYC activity in acute myeloid leukemia. *Nat*
1032 *Commun* **10**, 172 (2019). https://doi.org:10.1038/s41467-018-08076-y
1033 89 Seton-Rogers, S. RNA splicing: MYC maintains high-fidelity splicing. *Nat Rev Cancer* **15**, 385
1034 (2015). https://doi.org:10.1038/nrc3977
1035 90 Matera, A. G. & Wang, Z. A day in the life of the spliceosome. *Nat Rev Mol Cell Biol* **15**, 108-121
1036 (2014). https://doi.org:10.1038/nrm3742
1037 91 Wahl, M. C., Will, C. L. & Luhrmann, R. The spliceosome: design principles of a dynamic RNP
1038 machine. *Cell* **136**, 701-718 (2009). https://doi.org:10.1016/j.cell.2009.02.009
1039 92 Pan, Q., Shai, O., Lee, L. J., Frey, B. J. & Blencowe, B. J. Deep surveying of alternative splicing
1040 complexity in the human transcriptome by high-throughput sequencing. *Nat Genet* **40**, 1413-1415
1041 (2008). https://doi.org:10.1038/ng.259
1042 93 Wang, E. T. *et al.* Alternative isoform regulation in human tissue transcriptomes. *Nature* **456**, 470-
1043 476 (2008). https://doi.org:10.1038/nature07509
1044 94 Yang, X. *et al.* Widespread Expansion of Protein Interaction Capabilities by Alternative Splicing.
1045 *Cell* **164**, 805-817 (2016). https://doi.org:10.1016/j.cell.2016.01.029
1046 95 Liu, Y. *et al.* Impact of Alternative Splicing on the Human Proteome. *Cell Rep* **20**, 1229-1241
1047 (2017). https://doi.org:10.1016/j.celrep.2017.07.025
1048 96 Daemen, A. *et al.* Pan-Cancer Metabolic Signature Predicts Co-Dependency on Glutaminase and
1049 De Novo Glutathione Synthesis Linked to a High-Mesenchymal Cell State. *Cell Metab* **28**, 383-399
1050 e389 (2018). https://doi.org:10.1016/j.cmet.2018.06.003
1051 97 Redis, R. S. *et al.* Allele-Specific Reprogramming of Cancer Metabolism by the Long Non-coding
1052 RNA CCAT2. *Mol Cell* **61**, 520-534 (2016). https://doi.org:10.1016/j.molcel.2016.01.015
1053 98 Gong, C. *et al.* Sequential inverse dysregulation of the RNA helicases DDX3X and DDX3Y
1054 facilitates MYC-driven lymphomagenesis. *Mol Cell* (2021).
1055 https://doi.org:10.1016/j.molcel.2021.07.041
1056 99 Bosse, K. R. & Maris, J. M. Advances in the translational genomics of neuroblastoma: From
1057 improving risk stratification and revealing novel biology to identifying actionable genomic
1058 alterations. *Cancer* (2015). https://doi.org:10.1002/cncr.29706
1059 100 Pinto, N. R. *et al.* Advances in Risk Classification and Treatment Strategies for Neuroblastoma. *J*
1060 *Clin Oncol* **33**, 3008-3017 (2015). https://doi.org:10.1200/JCO.2014.59.4648
1061 101 Brodeur, G. M. Neuroblastoma: biological insights into a clinical enigma. *Nat Rev Cancer* **3**, 203-
1062 216 (2003). https://doi.org:10.1038/nrc1014
1063 102 Maris, J. M., Hogarty, M. D., Bagatell, R. & Cohn, S. L. Neuroblastoma. *Lancet* **369**, 2106-2120
1064 (2007). https://doi.org:10.1016/S0140-6736(07)60983-0
1065 103 Cohn, S. L. *et al.* The International Neuroblastoma Risk Group (INRG) classification system: an
1066 INRG Task Force report. *J Clin Oncol* **27**, 289-297 (2009).
1067 https://doi.org:10.1200/jco.2008.16.6785

1068 104 Suh, E. *et al.* Late mortality and chronic health conditions in long-term survivors of early-
1069 adolescent and young adult cancers: a retrospective cohort analysis from the Childhood Cancer
1070 Survivor Study. *Lancet Oncol* **21**, 421-435 (2020). https://doi.org:10.1016/S1470-2045(19)30800-9
1071 105 Nathan, P. C. *et al.* Health-related quality of life in adult survivors of childhood Wilms tumor or
1072 neuroblastoma: A report from the childhood cancer survivor study. *Pediatr Blood Cancer* **49**, 704-
1073 715 (2007). https://doi.org:10.1002/pbc.20949
1074 106 Brady, S. W. *et al.* Pan-neuroblastoma analysis reveals age- and signature-associated driver
1075 alterations. *Nat Commun* **11**, 5183 (2020). https://doi.org:10.1038/s41467-020-18987-4
1076 107 Han, T. *et al.* Anticancer sulfonamides target splicing by inducing RBM39 degradation via
1077 recruitment to DCAF15. *Science* **356** (2017). https://doi.org:10.1126/science.aal3755
1078 108 Xu, P., Duong, D. M. & Peng, J. Systematical optimization of reverse-phase chromatography for
1079 shotgun proteomics. *J Proteome Res* **8**, 3944-3950 (2009). https://doi.org:10.1021/pr900251d
1080 109 Bai, B. *et al.* U1 small nuclear ribonucleoprotein complex and RNA splicing alterations in
1081 Alzheimer's disease. *Proc Natl Acad Sci U S A* **110**, 16562-16567 (2013).
1082 https://doi.org:10.1073/pnas.1310249110
1083 110 Dobin, A. *et al.* STAR: ultrafast universal RNA-seq aligner. *Bioinformatics* **29**, 15-21 (2013).
1084 https://doi.org:10.1093/bioinformatics/bts635
1085 111 Shannon, P. *et al.* Cytoscape: a software environment for integrated models of biomolecular
1086 interaction networks. *Genome Res* **13**, 2498-2504 (2003). https://doi.org:10.1101/gr.1239303
1087

1088 **Figure Legends**

1089

1090

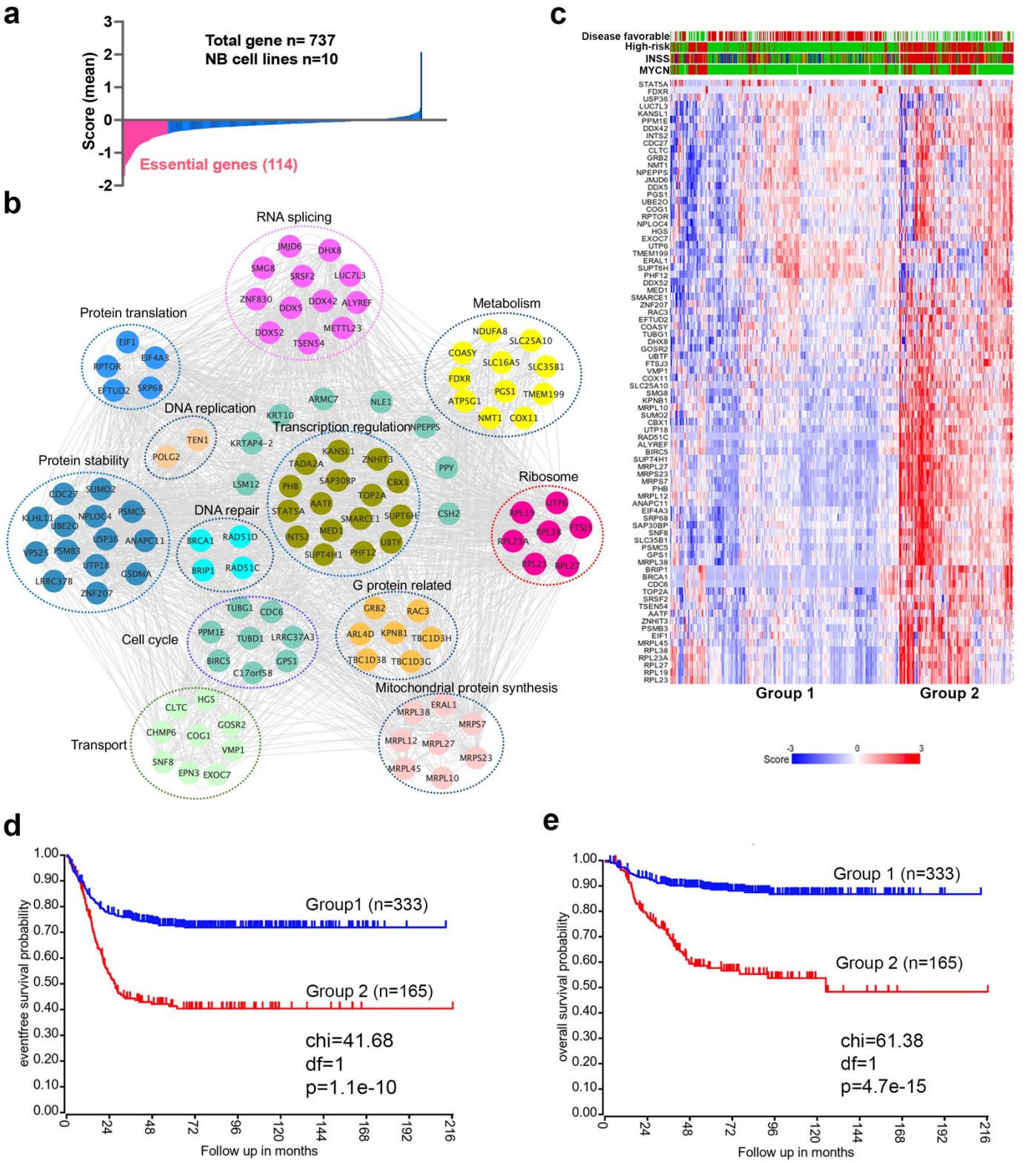

1091 **Figure 1. 17q contains neuroblastoma dependency genes**

1092 **a.** CRISPR score for 17q genes in 10 neuroblastoma cell lines. Score <-0.4 is defined as
1093 neuroblastoma dependency genes. Data are derived from Avana sgRNA library screening[63].
1094 **b.** STRING protein interaction network showing 17q essential genes with various biological
1095 functions.
1096 **c.** Heatmap by K-means clustering analysis showing 17q essential genes are highly expressed in
1097 high-risk neuroblastomas based on RNA-seq data (SEQC dataset).
1098 **d.** Kaplan-Meier survival curve showing 17q essential gene signature is correlated with worse
1099 event-free survival (SEQC dataset).
1100 **e.** Kaplan-Meier survival curve showing 17q essential gene signature is correlated with worse
1101 overall survival (SEQC dataset).
1102

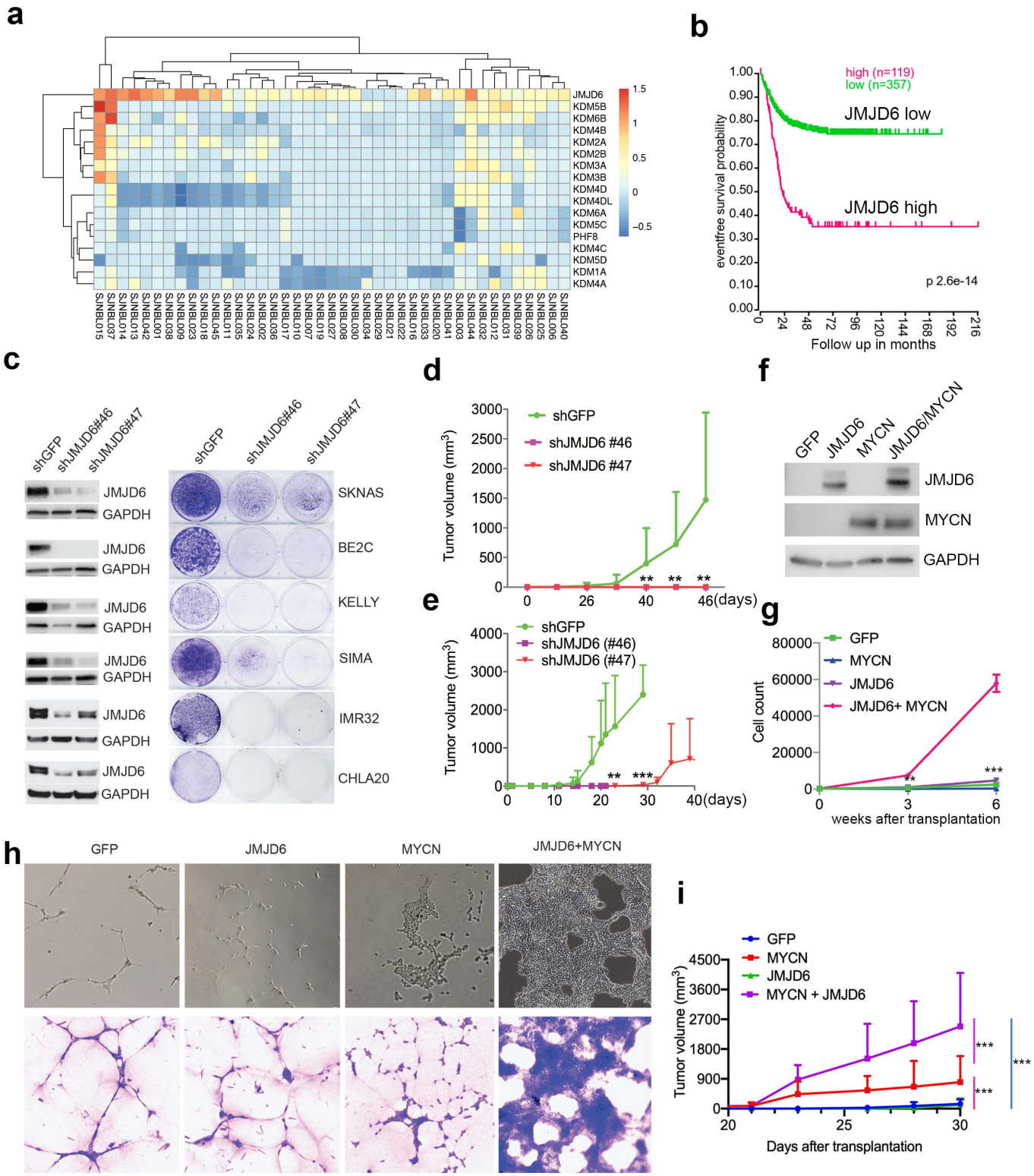

Figure 2. JMJD6 is required for neuroblastoma growth and facilitates MYC-mediated cellular transformation.

a. Copy number of genes encoding JmjC domain proteins in St Jude neuroblastoma cohort.

1109 **b.** Kaplan-Meier survival curve showing high JMJD6 is correlated with worse event-free survival
1110 (SEQC RNA-seq dataset).
1111 **c.** Crystal violet showing the colony staining on day 7 after JMJD6 shRNA knockdown in
1112 neuroblastoma cell lines validated by western blot (harvested at 72h).
1113 **d.** Xenograft tumor growth of BE2C (right) models with lentiviral JMJD6 shRNA knockdown. P-
1114 value calculated by multiple unpaired t-test across each row. n=5 per group.***p<0.001,
1115 **p<0.01.
1116 **e.** Xenograft tumor growth of SK-N-AS models with lentiviral JMJD6 shRNA knockdown. P- value
1117 calculated by multiple unpaired t-test across each row. ***p<0.001, **p<0.01.
1118 **f.** Western blot validating the expression of retroviral based MYCN and JMJD6 in JoMa1 cells.
1119 **g.** Cell proliferation of JoMa1 cells transduced with indicated constructs, GFP, JMJD6, MYCN,
1120 JMJD6+MYCN.
1121 **h.** Colony formation JoMa1 cells transduced with indicated constructs, GFP, JMJD6, MYCN,
1122 JMJD6+MYCN. Top panel showing photos taken under light microscope. Bottom panel showing
1123 cell colonies stained with crystal violet. P value calculated by multiple unpaired t-test across each
1124 row. ***p<0.001, **p<0.01.
1125 **i.** Xenograft tumor growth of JoMa1 cells transduced with indicated constructs, GFP, JMJD6, MYCN,
1126 JMJD6+MYCN. n=5 per group. P value calculated by multiple unpaired t-test across each row.
1127 ***p<0.001, **p<0.01.

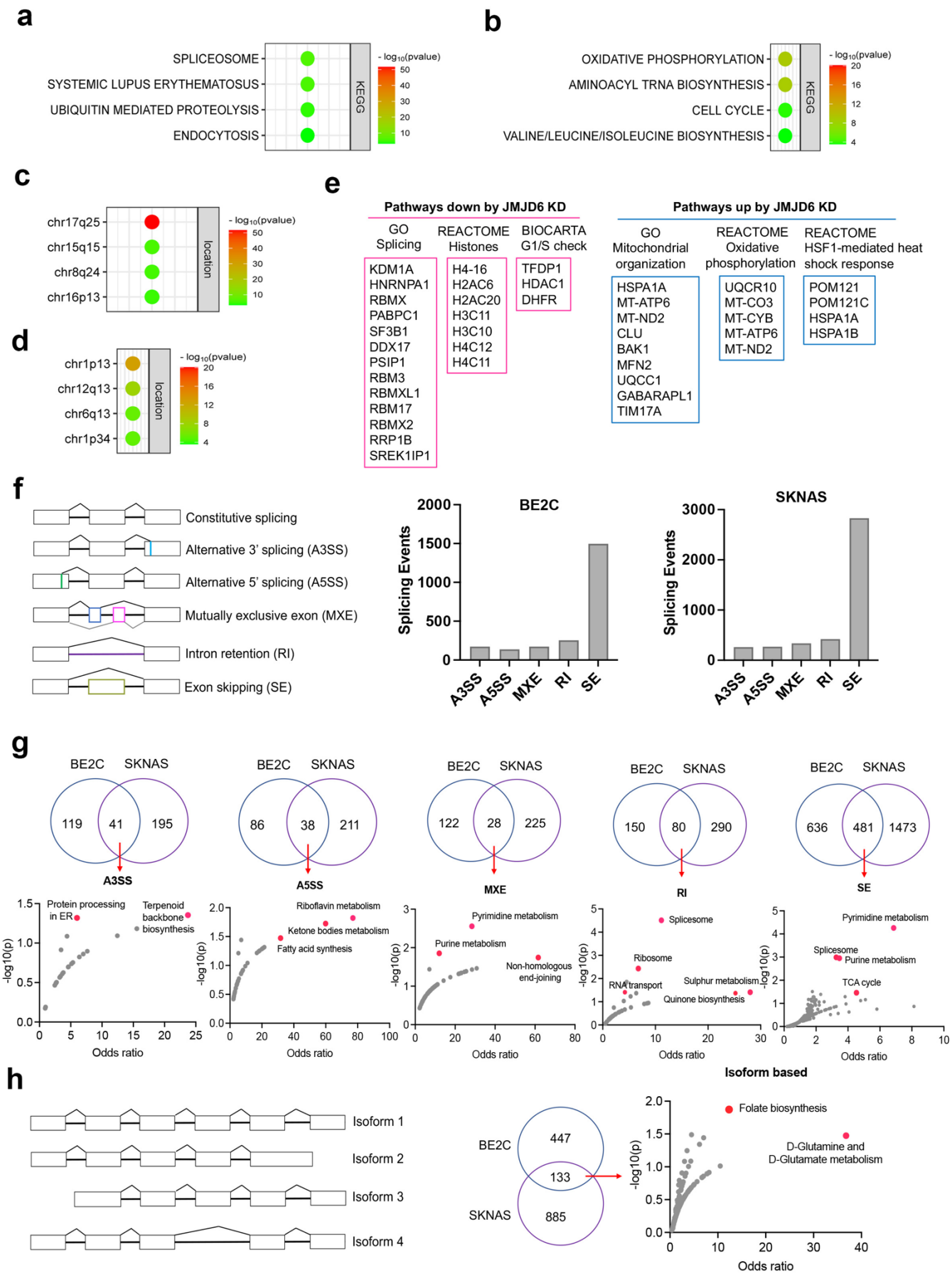
a
SPLICEOSOME
SYSTEMIC LUPUS ERYTHEMATOSUS
UBIQUITIN MEDIATED PROTEOLYSIS
ENDOCYTOSIS
KEGG
- log10(pvalue)
b
OXIDATIVE PHOSPHORYLATION
AMINOACYL TRNA BIOSYNTHESIS
CELL CYCLE
VALINE/LEUCINE/ISOLEUCINE BIOSYNTHESIS
c
chr17q25
chr15q15
chr8q24
chr16p13
location
d
chr1p13
chr12q13
chr6q13
chr1p34
e
Pathways down by JMJD6 KD
GO Splicing
KDM1A
HNRNPA1
RBMX
PABPC1
SF3B1
DDX17
PSIP1
RBM3
RBMXL1
RBM17
RBMX2
RRP1B
SREK1IP1
REACTOME Histones
H4-16
H2AC6
H2AC20
H3C11
H3C10
H4C12
H4C11
BIOCARTA G1/S check
TFDP1
HDAC1
DHFR
Pathways up by JMJD6 KD
GO Mitochondrial organization
HSPA1A
MT-ATP6
MT-ND2
CLU
BAK1
MFN2
UQCC1
GABARAPL1
TIM17A
REACTOME Oxidative phosphorylation
UQCR10
MT-CO3
MT-CYB
MT-ATP6
MT-ND2
REACTOME HSF1-mediated heat shock response
POM121
POM121C
HSPA1A
HSPA1B
f
Constitutive splicing
Alternative 3' splicing (A3SS)
Alternative 5' splicing (A5SS)
Mutually exclusive exon (MXE)
Intron retention (RI)
Exon skipping (SE)
BE2C
SKNAS
Splicing Events
A3SS
A5SS
MXE
RI
SE
g
BE2C
SKNAS
119
41
195
86
38
211
122
28
225
150
80
290
636
481
1473
Protein processing in ER
Terpenoid backbone biosynthesis
Riboflavin metabolism
Ketone bodies metabolism
Fatty acid synthesis
Pyrimidine metabolism
Purine metabolism
Non-homologous end-joining
Splicesome
Ribosome
RNA transport
Sulphur metabolism
Quinone biosynthesis
TCA cycle
-log10(p)
Odds ratio
h
Isoform 1
Isoform 2
Isoform 3
Isoform 4
Isoform based
447
133
885
Folate biosynthesis
D-Glutamine and D-Glutamate metabolism

1128 **Figure 3. JMJD6 regulates pre-mRNA splicing of genes involved in metabolism**

1129 **a.** Pathway enrichment for JMJD6 co-dependency genes whose knockout exhibits similar phenotype
1130 with JMJD6 knockout based on re-analysis of DepMAP data.

1131 **b.** Pathway enrichment for genes whose knockout exhibits opposite phenotype with JMJD6 knockout
1132 based on re-analysis of DepMAP data.

1133 **c.** Chromosomal location enrichment for JMJD6 co-dependency genes whose knockout exhibits
1134 similar phenotype with JMJD6 knockout based on re-analysis of DepMAP data.

1135 **d.** Chromosomal location enrichment for genes whose knockout exhibits opposite phenotype with
1136 JMJD6 knockout based on re-analysis of DepMAP data.

1137 **e.** Pathways analysis for genes downregulated and upregulated by JMJD6 knockdown commonly
1138 shared in SK-NAS and BE2C cells.

1139 **f.** Alternative splicing events altered by JMJD6 knockdown in BE2C and SK-N-AS cells.

1140 **g.** Pathway enrichment for each splicing event commonly shared in BE2C and SK-N-AS cells after
1141 JMJD6 knockdown.

1142 **h.** Isoform identification based on splicing events in BE2C and SK-N-AS cells, followed by pathway
1143 enrichment for commonly shared alterations in both cell lines.

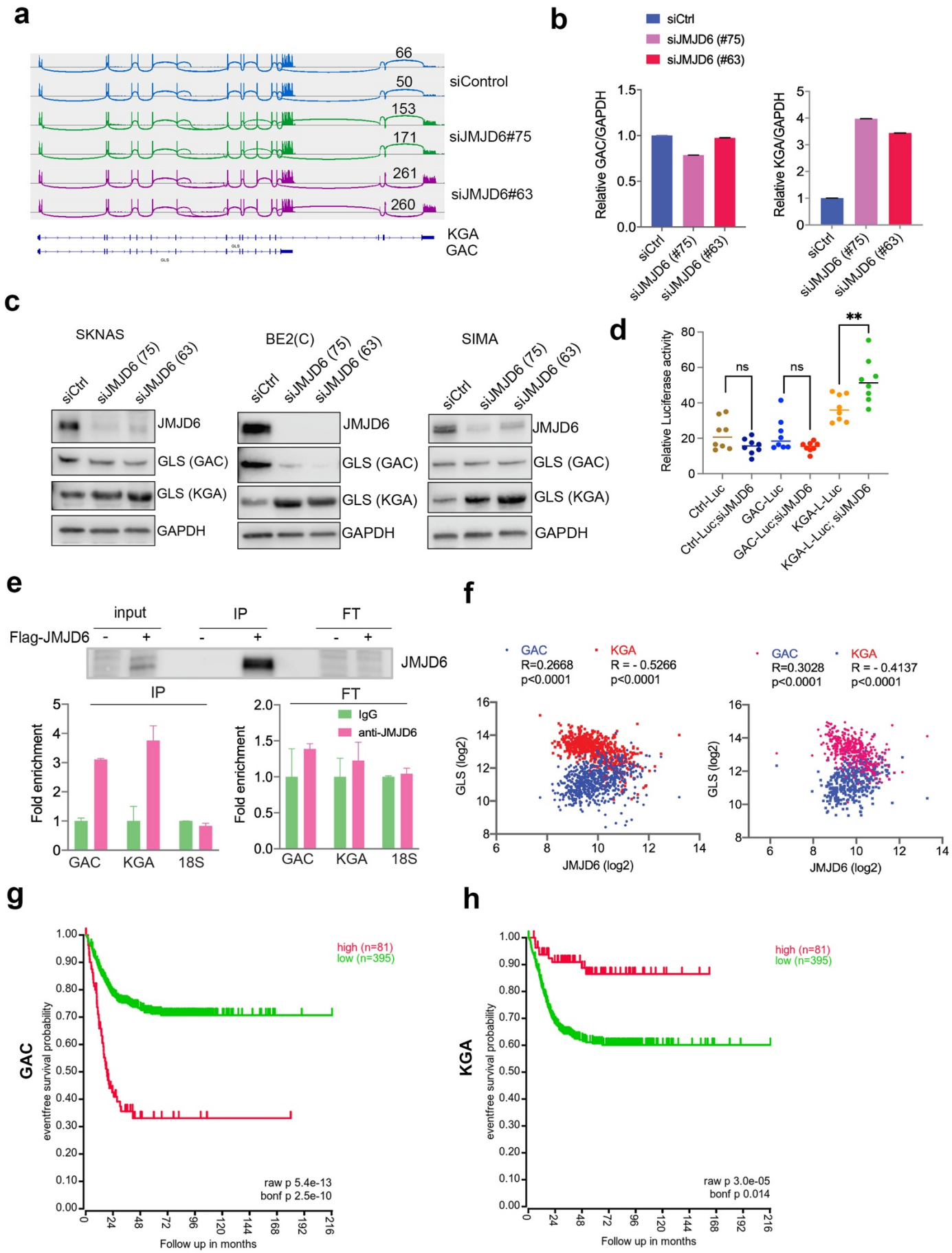
a
66
50
siControl
153
171
siJMJD6#75
261
siJMJD6#63
260
KGA
GAC
b
siCtrl
siJMJD6 (#75)
siJMJD6 (#63)
Relative GAC/GAPDH
Relative KGA/GAPDH
c
SKNAS
BE2(C)
SIMA
siCtrl
siJMJD6 (75)
siJMJD6 (63)
JMJD6
GLS (GAC)
GLS (KGA)
GAPDH
d
Relative Luciferase activity
ns
**
Ctrl-Luc
Ctrl-Luc;siJMJD6
GAC-Luc
GAC-Luc;siJMJD6
KGA-L-Luc
KGA-L-Luc; siJMJD6
e
input
IP
FT
Flag-JMJD6
JMJD6
Fold enrichment
IgG
anti-JMJD6
GAC
KGA
18S
f
GAC
R=0.2668
p<0.0001
KGA
R = - 0.5266
p<0.0001
R=0.3028
p<0.0001
R = - 0.4137
p<0.0001
GLS (log2)
JMJD6 (log2)
g
high (n=81)
low (n=395)
eventfree survival probability
raw p 5.4e-13
bonf p 2.5e-10
Follow up in months
h
raw p 3.0e-05
bonf p 0.014

1144

1145 **Figure 4. JMJD6 regulates alternative splicing of glutaminolysis gene, GLS**

1146 **a.** Sashimi plot showing the alternative splicing of *GLS* after JMJD6 knockdown in BE2C cells in
1147 duplicates. The number indicates the RNA-seq read counts of exon junction.

1148 **b.** Real time PCR assessing the relative expression of *GAC* and *KGA* isoforms after JMJD6
1149 knockdown in BE2C cells in triplicates.

1150 **c.** Western blot showing the expression of GAC and KGA isoforms in SK-N-AS, BE2C, SIMA
1151 after JMJD6 knockdown for 72 hours.

1152 **d.** KGA and GAC specific reporter analysis showing only KGA-driven luciferase activity is
1153 significantly upregulated by JMJD6 knockdown.

1154 **e.** RNA-immunoprecipitation showing JMJD6 interaction with *GLS* RNA. Top panel shows the
1155 western blot analysis of Flag tagged JMJD6 in input, immunoprecipitation (IP) and flowthrough
1156 (FT)_fractions. Bottom panel shows RT PCR analysis of enrichment of GAC/KGA bound by
1157 JMJD6 in IP and FT fractions.

1158 **f.** Spearman correlation analysis of *JMJD6* and *GAC*/*KGA* expression levels in two neuroblastoma
1159 cohorts GSE45547(left) and GSE120572 (right).

1160 **g.** Kaplan-Meier curve showing the association of high or low *GAC* expression levels with event-
1161 free survival in a cohort of neuroblastoma (GSE45547).

1162 **h.** Kaplan-Meier curve showing the association of high or low *KGA* expression levels with event-
1163 free survival in a cohort of neuroblastoma (GSE45547).

1164
1165
1166
1167
1168
1169
1170
1171
1172
1173
1174

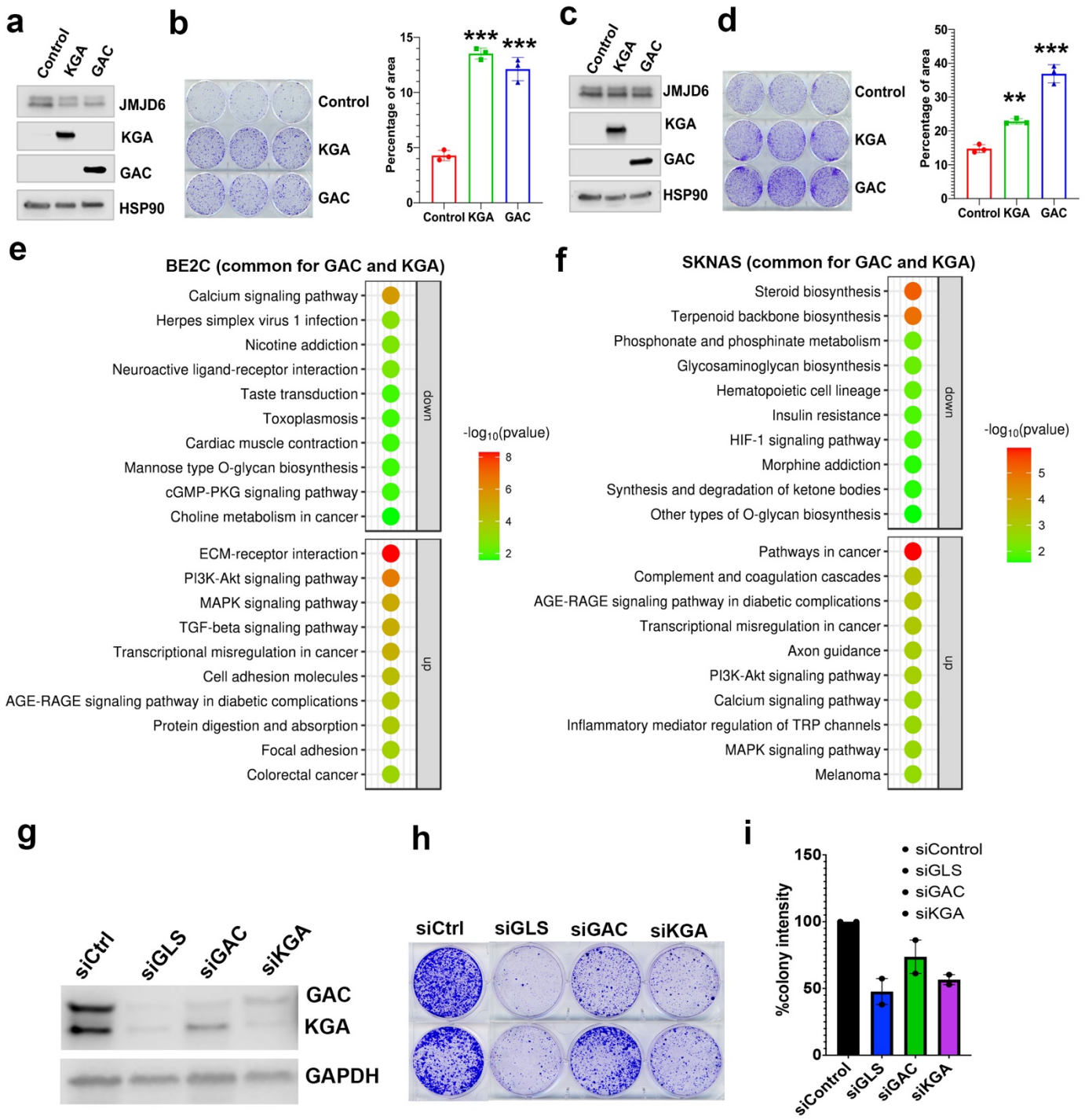

Figure 5. GAC and KGA are both important for cell survival

a. Western blotting analysis of expression of KGA and GAC in BE2C cells with indicated antibodies.

1182 b. Colony formation assay for BE2C cells overexpressing KGA and GAC for 7 days (left =crystal
1183 violet staining, right = quantification of cell density).). N=3 per group. ***p<0.001.
1184 c. Western blotting analysis of expression of KGA and GAC in SK-N-AS cells with indicated
1185 antibodies.
1186 d. Colony formation assay for SK-N-AS cells overexpressing KGA and GAC for 7 days (left
1187 =crystal violet staining, right = quantification of cell density). N=3 per group. **p<0.01.
1188 ***p<0.001.
1189 e. Bubble blot showing the pathways significantly upregulated and downregulated by both KGA and
1190 GAC in BE2C cells.
1191 f. Bubble blot showing the pathways significantly upregulated and downregulated by both KGA and
1192 GAC in SKNAS cells.
1193 g. Whole cell lysates (on 72h) subject to Western blot showing the knockdown of GLS (both GAC
1194 and KGA), GAC alone and KGA alone in BE2C cells.
1195 h. Colony forming assay (on day 7) od BE2C cells with knockdown of GLS (both GAC and KGA),
1196 GAC alone and KGA alone. two independent experiments.
1197 i. Quantification of colonies in h using ImageJ software.

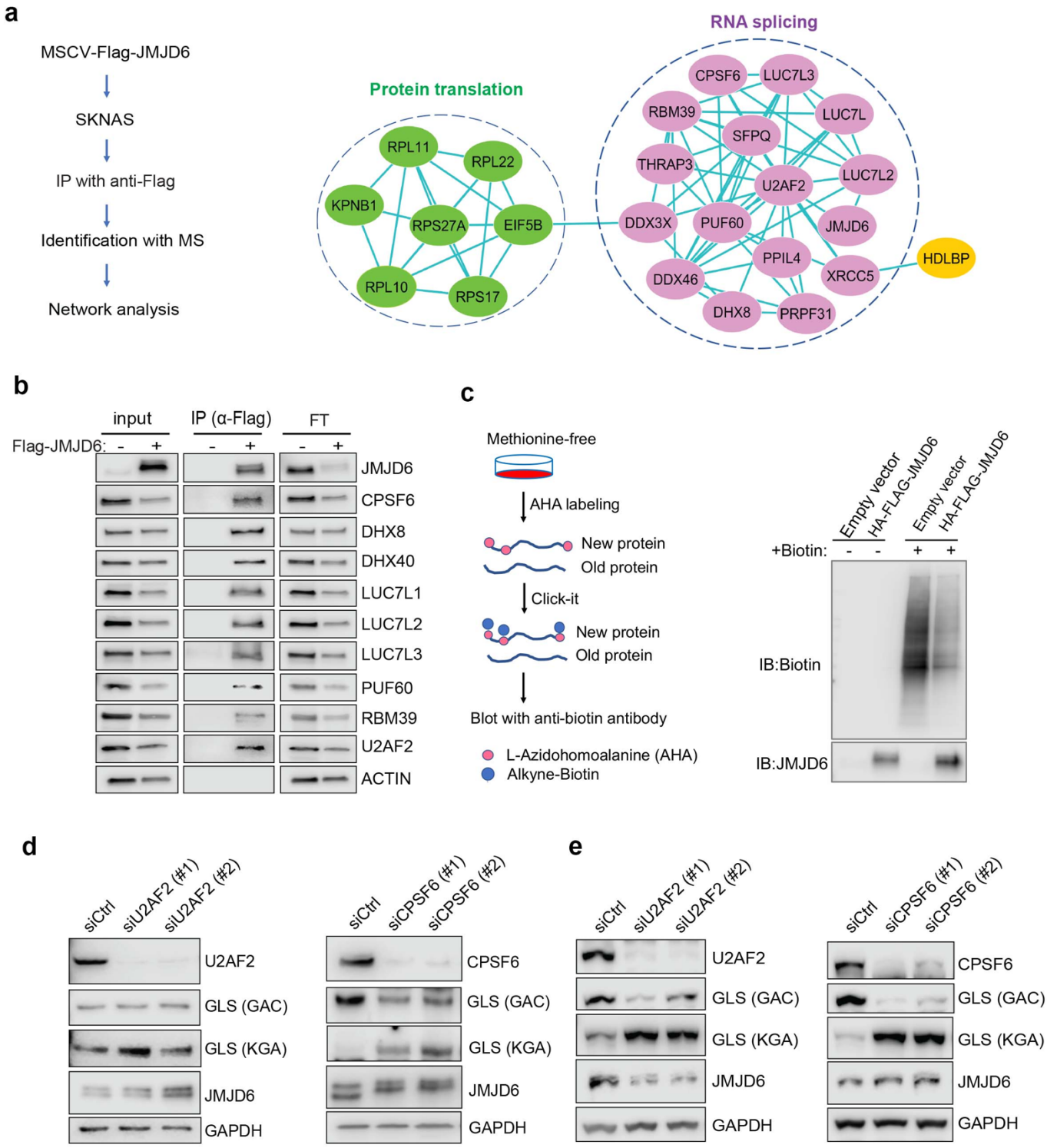
a
MSCV-Flag-JMJD6
SKNAS
IP with anti-Flag
Identification with MS
Network analysis
Protein translation
RPL11
RPL22
KPNB1
RPS27A
EIF5B
RPL10
RPS17
RNA splicing
CPSF6
LUC7L3
RBM39
LUC7L
SFPQ
THRAP3
U2AF2
LUC7L2
DDX3X
PUF60
JMJD6
PPIL4
HDLBP
DDX46
XRCC5
DHX8
PRPF31
b
input
IP (α-Flag)
FT
Flag-JMJD6: - + - + - +
JMJD6
CPSF6
DHX8
DHX40
LUC7L1
LUC7L2
LUC7L3
PUF60
RBM39
U2AF2
ACTIN
c
Methionine-free
AHA labeling
New protein
Old protein
Click-it
New protein
Old protein
Blot with anti-biotin antibody
L-Azidohomoalanine (AHA)
Alkyne-Biotin
Empty vector
HA-FLAG-JMJD6
Empty vector
HA-FLAG-JMJD6
+Biotin: - - + +
IB:Biotin
IB:JMJD6
d
siCtrl
siU2AF2 (#1)
siU2AF2 (#2)
U2AF2
GLS (GAC)
GLS (KGA)
JMJD6
GAPDH
siCtrl
siCPSF6 (#1)
siCPSF6 (#2)
CPSF6
GLS (GAC)
GLS (KGA)
JMJD6
GAPDH
e
siCtrl
siU2AF2 (#1)
siU2AF2 (#2)
U2AF2
GLS (GAC)
GLS (KGA)
JMJD6
GAPDH
siCtrl
siCPSF6 (#1)
siCPSF6 (#2)
CPSF6
GLS (GAC)
GLS (KGA)
JMJD6
GAPDH

1198

1199 **Figure 6. JMJD6 forms an interaction network consists of proteins involved in splicing and protein**
1200 **synthesis**

1201 **a.** Flag tagged JMJD6 transduced into SK-N-AS cells for immunoprecipitation with anti-Flag
1202 followed by protein identification by mass spectrometry. The interacting protein partners of
1203 JMJD6 are analyzed by STRING protein network.

1204 **b.** Immunoprecipitation followed by western blot to validate the JMJD6 interacting partners in
1205 SK-N-AS cells. IP= immunoprecipitation, FT= flowthrough.

1206 **c.** Click-IT AHA labeling showing the newly synthesized proteins after overexpression of
1207 JMJD6 in SK-N-AS cells.

1208 **d,e.** Western blot showing the expression of GAC and KGA isoforms in BE2C (d) SK-N-AS (e),
1209 after U2AF2 and CPSF6 knockdown for 72hours.

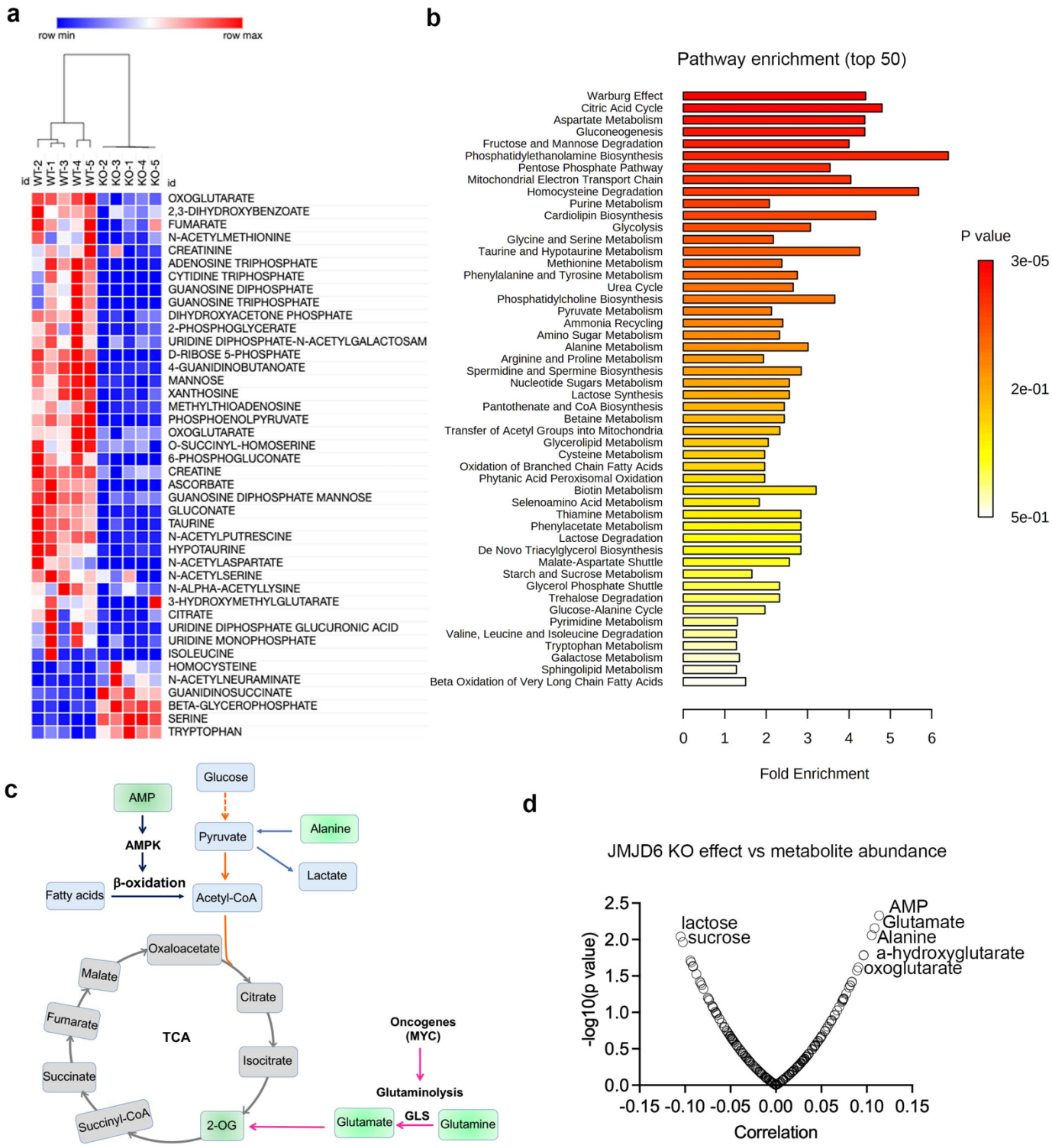
a
row min
row max
id
WT-2
WT-1
WT-3
WT-4
WT-5
KO-2
KO-3
KO-1
KO-4
KO-5
OXOGLUTARATE
2,3-DIHYDROXYBENZOATE
FUMARATE
N-ACETYLMETHIONINE
CREATININE
ADENOSINE TRIPHOSPHATE
CYTIDINE TRIPHOSPHATE
GUANOSINE DIPHOSPHATE
GUANOSINE TRIPHOSPHATE
DIHYDROXYACETONE PHOSPHATE
2-PHOSPHOGLYCERATE
URIDINE DIPHOSPHATE-N-ACETYLGALACTOSAM
D-RIBOSE 5-PHOSPHATE
4-GUANIDINOBUTANOATE
MANNOSE
XANTHOSINE
METHYLTHIOADENOSINE
PHOSPHOENOLPYRUVATE
OXOGLUTARATE
O-SUCCINYL-HOMOSERINE
6-PHOSPHOGLUCONATE
CREATINE
ASCORBATE
GUANOSINE DIPHOSPHATE MANNOSE
GLUCONATE
TAURINE
N-ACETYLPUTRESCINE
HYPOTAURINE
N-ACETYLASPARTATE
N-ACETYLSERINE
N-ALPHA-ACETYLLYSINE
3-HYDROXYMETHYLGLUTARATE
CITRATE
URIDINE DIPHOSPHATE GLUCURONIC ACID
URIDINE MONOPHOSPHATE
ISOLEUCINE
HOMOCYSTEINE
N-ACETYLNEURAMINATE
GUANIDINOSUCCINATE
BETA-GLYCEROPHOSPHATE
SERINE
TRYPTOPHAN
b
Pathway enrichment (top 50)
Warburg Effect
Citric Acid Cycle
Aspartate Metabolism
Gluconeogenesis
Fructose and Mannose Degradation
Phosphatidylethanolamine Biosynthesis
Pentose Phosphate Pathway
Mitochondrial Electron Transport Chain
Homocysteine Degradation
Purine Metabolism
Cardiolipin Biosynthesis
Glycolysis
Glycine and Serine Metabolism
Taurine and Hypotaurine Metabolism
Methionine Metabolism
Phenylalanine and Tyrosine Metabolism
Urea Cycle
Phosphatidylcholine Biosynthesis
Pyruvate Metabolism
Ammonia Recycling
Amino Sugar Metabolism
Alanine Metabolism
Arginine and Proline Metabolism
Spermidine and Spermine Biosynthesis
Nucleotide Sugars Metabolism
Lactose Synthesis
Pantothenate and CoA Biosynthesis
Betaine Metabolism
Transfer of Acetyl Groups into Mitochondria
Glycerolipid Metabolism
Cysteine Metabolism
Oxidation of Branched Chain Fatty Acids
Phytanic Acid Peroxisomal Oxidation
Biotin Metabolism
Selenoamino Acid Metabolism
Thiamine Metabolism
Phenylacetate Metabolism
Lactose Degradation
De Novo Triacylglycerol Biosynthesis
Malate-Aspartate Shuttle
Starch and Sucrose Metabolism
Glycerol Phosphate Shuttle
Trehalose Degradation
Glucose-Alanine Cycle
Pyrimidine Metabolism
Valine, Leucine and Isoleucine Degradation
Tryptophan Metabolism
Galactose Metabolism
Sphingolipid Metabolism
Beta Oxidation of Very Long Chain Fatty Acids
P value
3e-05
2e-01
5e-01
0
1
2
3
4
5
6
Fold Enrichment
c
Glucose
AMP
AMPK
Pyruvate
Alanine
Lactate
β-oxidation
Fatty acids
Acetyl-CoA
Oxaloacetate
Malate
Citrate
Fumarate
TCA
Isocitrate
Succinate
Succinyl-CoA
2-OG
Oncogenes
(MYC)
Glutaminolysis
Glutamate
GLS
Glutamine
d
JMJD6 KO effect vs metabolite abundance
lactose
sucrose
AMP
Glutamate
Alanine
a-hydroxyglutarate
oxoglutarate
-log10(p value)
2.5
2.0
1.5
1.0
0.5
0.0
-0.15
-0.10
-0.05
0.00
0.05
0.10
0.15
Correlation

1210

1211 **Figure 7. JMJD6 regulates production of citric acid cycle intermediates and NTP**

1212 **a.** Heatmap showing the metabolites differentially expressed in SK-N-AS cells (n=5) after
1213 JMJD6 knockout (n=5) based on LC-MS/MS analysis.

1214 **b.** Pathway analysis of metabolites downregulated by JMJD6 knockout.

1215 **c.** Pathway cartoon showing the connections of TCA, glycolysis, glutaminolysis, and β-
1216 oxidation.

1217 **d.** Correlation of metabolite abundance with JMJD6 dependency. The positive correlation
1218 indicates that the higher the abundance of metabolites, the more resistance of cells to JMJD6
1219 knockout. On the contrary, the negative correlation indicates the higher the abundance of
1220 metabolites, the more sensitive of cells to JMJD6 knockout.

1221

1222

1223

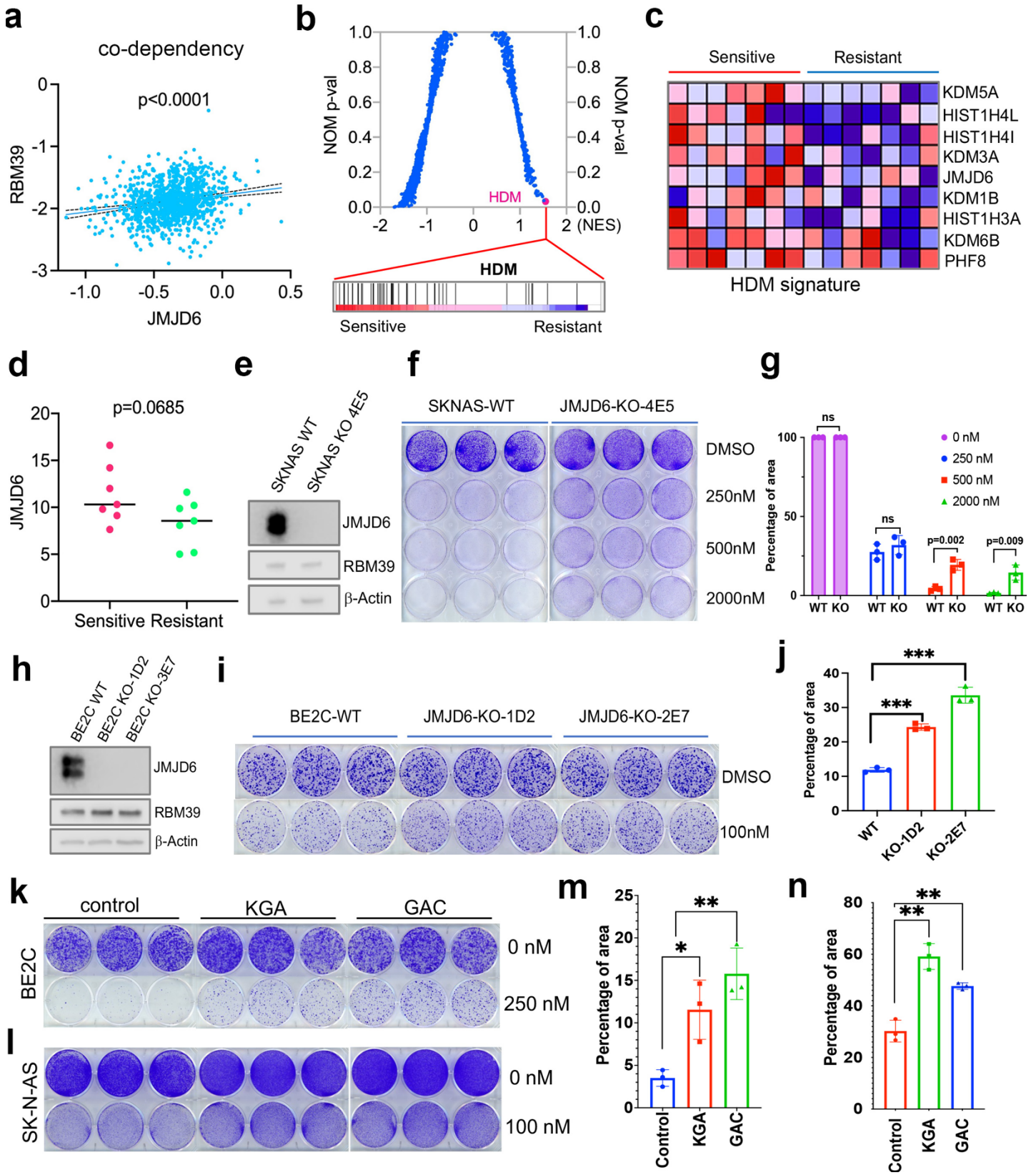
a
co-dependency
p<0.0001
RBM39
JMJD6
b
NOM p-val
HDM
2 (NES)
HDM
Sensitive
Resistant
c
Sensitive
Resistant
KDM5A
HIST1H4L
HIST1H4I
KDM3A
JMJD6
KDM1B
HIST1H3A
KDM6B
PHF8
HDM signature
d
p=0.0685
JMJD6
Sensitive Resistant
e
SKNAS WT
SKNAS KO 4E5
JMJD6
RBM39
β-Actin
f
SKNAS-WT
JMJD6-KO-4E5
DMSO
250nM
500nM
2000nM
g
Percentage of area
ns
ns
p=0.002
p=0.009
0 nM
250 nM
500 nM
2000 nM
WT KO WT KO WT KO WT KO
h
BE2C WT
BE2C KO-1D2
BE2C KO-3E7
JMJD6
RBM39
β-Actin
i
BE2C-WT
JMJD6-KO-1D2
JMJD6-KO-2E7
DMSO
100nM
j
Percentage of area
***
***
WT
KO-1D2
KO-2E7
k
control
KGA
GAC
BE2C
0 nM
250 nM
l
SK-N-AS
0 nM
100 nM
m
Percentage of area
**
*
Control
KGA
GAC
n
Percentage of area
**
**
Control
KGA
GAC

1228 **Figure 8. JMJD6-GAC pathway regulates the response of neuroblastoma cells to indisulam treatment**

1229 **a.** Spearman correlation of effects of JMJD6 knockout and RBM39 knockout demonstrating the
1230 co-dependency of JMJD6 and RBM39 from DepMAP CRISPR screening data (n=1086). Each
1231 dot represents one cell line.

1232 **b.** GSEA analysis for indisulam sensitive vs resistant neuroblastoma cell lines based on CTD2
1233 (Cancer Target Discovery and Development) data showing histone lysine demethylase gene
1234 signature is the one that is significantly associated with indisulam response.

1235 **c.** Heatmap from GSEA (b) showing the individual genes in indisulam sensitive and resistant cells.

1236 **d.** JMJD6 expression in indisulam sensitive and resistant neuroblastoma cells. p value calculated
1237 by student t test.

1238 **e.** Western blot showing JMJD6 knockout in SK-N-AS cells using indicated antibodies.

1239 **f.** Colony formation of SK-N-AS cells in triplicates with or without JMJD6 knockout treated with
1240 different concentrations of indisulam for 7 days, stained with crystal violet. N=3 per group.

1241 **g.** Quantification of cell density by using ImageJ software from f. ns=not significant. ** $p<0.001$,
1242 ***$p<0.0001$

1243 **h.** Western blot showing JMJD6 knockout in BE2C cells using indicated antibodies.

1244 **i.** Colony formation of BE2C cells in triplicates with or without JMJD6 knockout treated with
1245 100nM of indisulam for 5 days, stained with crystal violet. N=3 per group.

1246 **j.** Quantification of cell density by using ImageJ software from f. ns=not significant. ** $p<0.001$,
1247 ***$p<0.0001$

1248 **k.** Colony formation of BE2C cells in triplicates with KGA and GAC overexpression treated with
1249 250nM of indisulam for 5 days, stained with crystal violet. N=3 per group.

1250 **l.** Colony formation of SK-N-AS cells in triplicates with KGA and GAC overexpression treated
1251 with 100nM of indisulam for 7 days, stained with crystal violet.

1252 **m.** Quantification of cell density by using ImageJ software from k. * $p<0.01$, **$p<0.001$

1253 **n.** Quantification of cell density by using ImageJ software from l. **$p<0.001$

1254

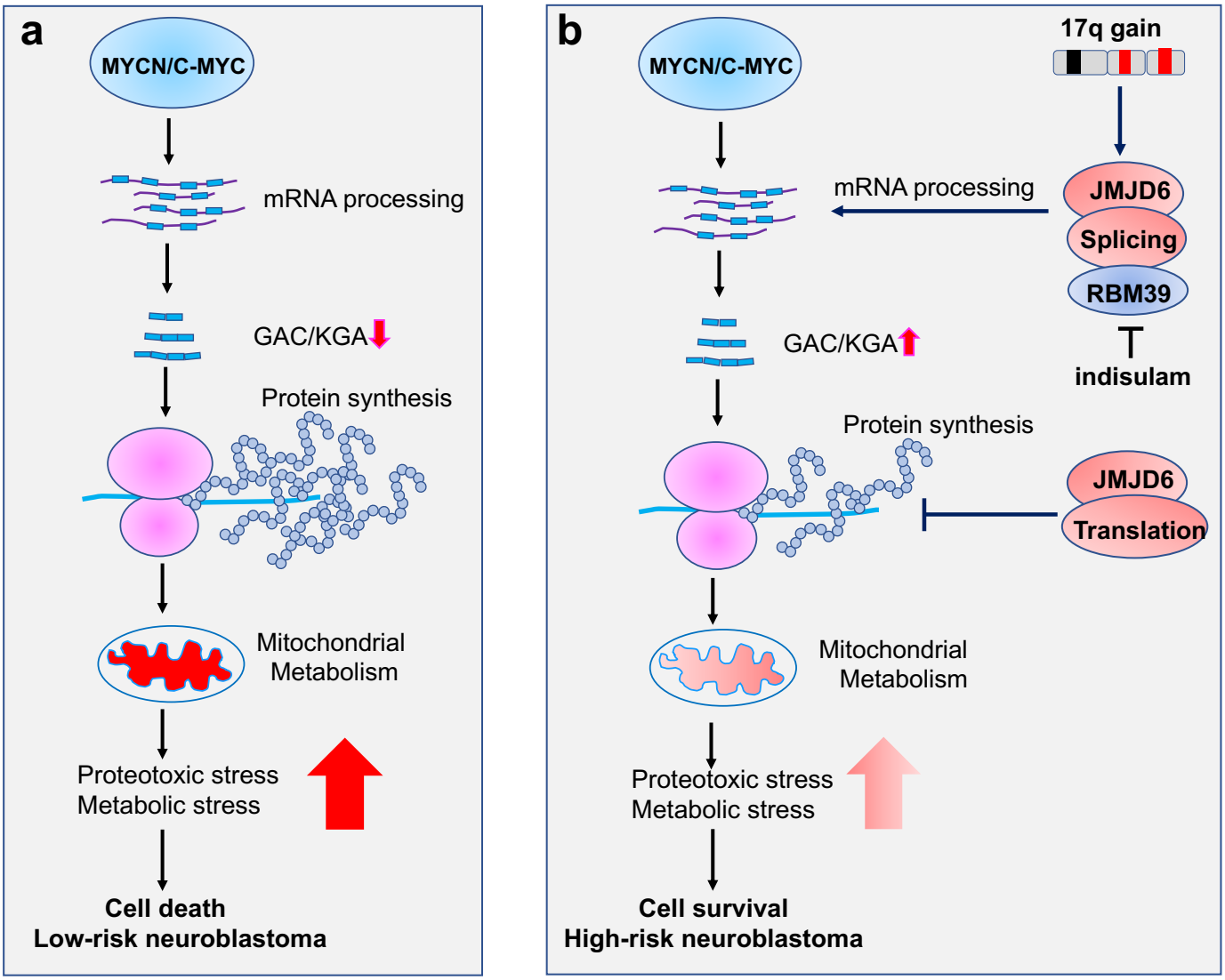

1255

1256

1257 **Figure 9. Working mechanism of JMJD6 in MYC-driven neuroblastoma.** Overactive MYC drives
1258 high-load of gene transcription, enhanced protein synthesis and high rate of metabolism, leading to
1259 detrimental cellular stresses and consequent cell death (**Model a**). However, when 17q is amplified, high
1260 levels of JMJD6 and other proteins encoded by 17q genes physically interacts with the splicing and
1261 translational machineries, enhancing pre-mRNA splicing of metabolic genes such as GLS and inhibiting
1262 global protein synthesis, respectively, leading to reduced detrimental stresses and enhanced cancer cell
1263 survival and tumorigenesis (**Model b**). The high levels of JMJD6 predicts high dependency of RBM39,
1264 which are more sensitive to indisulam treatment.